Structural insights into Crimean-Congo haemorrhagic fever virus RNA polymerase reveal a dual-site non-nucleoside inhibition mechanism

Kankan Yang[1,#], Haiqiang Wu[1,2,#], Xunbi Liu[1,2,#], Zuxing Liang[3], Junwei Zou[1], Yong Wang[2], Jun Ma[1,*]

[1]Institute of Infectious Diseases, Shenzhen Bay Laboratory, Shenzhen, 518132, China

[2]College of Veterinary Medicine, Anhui Agricultural University, Hefei, 230036, China

[3]College of Life Science, Capital Normal University, Beijing, 100875, China

[#]These authors contributed equally: Kankan Yang, Haiqiang Wu, Xunbi Liu

*Correspondence: Jun Ma (majun@szbl.ac.cn)

Abstract

Crimean-Congo hemorrhagic fever virus (CCHFV) is a priority pathogen defined by its wide geographic distribution and high case-fatality rates, yet no approved vaccines or therapeutics exist. Its massive ~450 kDa RNA-dependent RNA polymerase (L protein)—the multi-domain and multi-functional machinery for viral transcription and replication—has remained structurally enigmatic due to its exceptional size and complexity. Here we present cryo-EM structures of the CCHFV L protein in apo, promoter-bound, and inhibitor-bound states. Structural analysis reveals that the L protein adopts the canonical architecture shared across the order *Bunyavirales*, with high structural conservation extending to individual subdomains and the 'hook-like' recognition of the vRNA promoter. Unexpectedly, we found that the non-nucleotide inhibitor suramin inhibits the polymerase through a unique dual-site mechanism. It not only competitively occludes the 5' vRNA-binding pocket but also functions as a “molecular glue” at the distal Linker–Fingers interface, likely allosterically restricting essential conformational dynamics. These findings provide a detailed structural framework for CCHFV replication and offer a novel paradigm for designing antivirals against *Bunyavirales*.

Key words

Crimean-Congo hemorrhagic fever virus, RNA-dependent RNA polymerase, Cryo-EM, viral replication, suramin

Introduction

Crimean-Congo hemorrhagic fever virus (CCHFV), the causative agent of Crimean-Congo hemorrhagic fever, is an enveloped, negative-sense single-stranded RNA virus (NSV) belonging to the genus *Nairovirus* within the order *Bunyavirales*. The disease manifests as an acute infectious syndrome primarily transmitted through *Hyalomma* tick bites, with secondary transmission occurring via contact with infected blood or body fluids[1-3]. Clinical manifestations include high fever, hemorrhagic signs, and hepatic/renal impairment, with case-fatality rates approaching 40%[4-6]. CCHFV is geographically widespread, being endemic in nearly 50 countries across Africa, Europe, Asia and the Middle East[7]. Given its high pathogenicity, epidemic potential, and the expanding geographic range of its tick vector under climate change, the World Health Organization (WHO) has designated CCHFV a priority pathogen requiring urgent countermeasure development[1,8]. Classified as a biosafety level 4 (BSL-4) agent, no approved vaccines or specific antiviral therapies currently exist for CCHFV. Moreover, the accelerating discovery of novel human pathogens within the genus *Orthonairovirus*—including Songling[9], Wetland[10], and Xuecheng[11] viruses—underscores the urgent need to develop effective therapeutic interventions.

The CCHFV genome comprises three RNA segments encoding the nucleoprotein (S segment), glycoproteins (M segment), and a large RNA-dependent RNA polymerase (RdRp or L protein)[12]. The L protein is a multi-domain and multifunctional enzyme that catalyzes viral RNA replication and transcription, and possesses cap-snatching activity[5,13]. Structural and functional insights have thus far been largely confined to the endonuclease domain[14] and the N-terminal ovarian tumour (OTU)-like domain[15-18], which exhibits deubiquitinating and deISGylating activities that counteract RIG-I-mediated innate immunity. Given its central role in viral replication, the RNA polymerase represents a prime target for antiviral development. Determining the high-resolution structure and mechanistic details of this viral RNA polymerase is therefore crucial for rational inhibitor design. In recent years, structures of L proteins from several highly pathogenic members of the *Bunyavirales*—including arenaviruses (e.g., Machupo virus [MACV][19-21] and Lassa virus [LASV][19,22]), hantaviruses (e.g., Hantaan virus [HTNV][23-25]), peribunyaviruses (e.g., La Crosse virus [LACV][26-28]), phenuiviruses (e.g., severe fever with thrombocytopenia syndrome virus

[SFTSV][29-31] and Rift Valley fever virus [RVFV])[32], the plant-infecting tospovirus tomato spotted wilt virus (TSWV)[33]—have been solved, significantly advancing our understanding of replication mechanisms across the order.

However, as a representative member of the family *Nairoviridae*, CCHFV encodes one of the largest known RNA polymerases, containing 3,945 residues with a molecular weight (MW) of approximately 450 kDa—nearly twice the size of typical bunyaviral L proteins. The exceptionally large size of the full-length L protein makes its expression, purification, and structural determination profoundly challenging. Consequently, the architecture and functional mechanisms of this giant polymerase remain unknown due to the lack of high resolution structural information, a gap that has impeded structure-based antiviral design.

Here we report the cryo-electron microscopy (cryo-EM) structures of the CCHFV L protein in three functional states: the apo form (2.59 Å), the 5' vRNA promoter-bound state (2.75 Å), and in complex with the non-nucleotide inhibitor suramin (2.5 Å). These structures reveal the architecture of the polymerase core, the mechanism of viral RNA promoter recognition, and a unique dual-site inhibitory mechanism for suramin. Together with functional assays of suramin derivatives, our work provides a structural foundation for developing antiviral strategies targeting the CCHFV polymerase.

Results

Cryo-EM structure of the CCHFV RNA-dependent RNA polymerase

The full-length CCHFV L protein (3,945 amino acids; ~450 kDa) (Fig. 1a) poses a considerable challenge for recombinant expression and purification due to its large size. After evaluating multiple expression strategies, we successfully expressed the full-length protein carrying a C-terminal Twin-Strep tag in mammalian HEK293F cells. Following purification by Strep-Tactin affinity and size-exclusion chromatography (SEC), the protein eluted as a homogeneous, monodisperse peak corresponding to approximately 450 kDa, consistent with SDS-PAGE analysis (Supplementary Fig. 1a, b).

Initial attempts to detect RNA-dependent RNA polymerase (RdRp) activity using the wild-type protein were compromised by intrinsic endonuclease activity. To establish a robust assay, we generated an endonuclease-inactivated mutant by alanine substitutions

of key catalytic residues (K835A/D839A/K842A) to eliminate potential template degradation. This mutant was purified using the same procedure as the wild-type protein. In a fluorescence-based primer-extension assay with a 26-nt 3' vRNA template and a 15-nt 5'-FAM-labeled primer, the mutant efficiently catalyzed RNA synthesis, generating extension products exceeding 25 nt (Supplementary Fig. 1c, d). This result confirms that the purified CCHFV L protein possesses authentic RdRP activity and establishes a robust assay for subsequent mechanistic and inhibitory studies.

Single-particle cryo-EM analysis of the CCHFV L protein in the apo state yielded a reconstruction at a global resolution of 2.59 Å (Fig. 1b and Supplementary Fig. 2). The final atomic model encompasses residues 928–3227; a large internal segment (residues 1901–2222) and several flexible loops remain unresolved (Fig. 1c). To date, only the N-terminal OTU (residues 1–159) and endonuclease (residues 584–927) domains have been structurally defined, whereas the C-terminal region (residues 3228–3945) remains poorly understood. Consistent with observations in other bunyaviral L proteins, the N- and C-terminal auxiliary domains are invisible in the apo state, likely becoming ordered only upon specific triggers such as viral RNA promoter or cofactor binding.

Structural architecture and conservation of the CCHFV L polymerase core

The well-resolved core region of the CCHFV L protein adopts the canonical architecture shared with other bunyaviral polymerases, comprising an N-terminal PA-like domain, a central PB1-like domain, and a C-terminal PB2-like domain (Fig. 1a). Specifically, the PA-like domain contains the Linker, Arch, vRBL (viral RNA-binding lobe), and Core lobe; the PB1-like domain forms the catalytic core, housing the Fingers, Palm, Thumb subdomains along with priming loop; and the PB2-like domain consists of the Bridge, thumb ring, and Lid. Structural comparisons reveal strong conservation of this core fold with RNA polymerases from other members of the order *Bunyavirales*, including SFTSV (*Phenuiviridae*), LACV (*Bunyaviridae*), HTNV (*Hantaviridae*), as well as LASV and MACV (*Arenaviridae*) (Fig. 2a). Within this conserved core, individual functional subdomains (vRBL, Fingers, Palm, Core lobe, and Thumb-thumb ring) share highly similar architectures, although the Core lobe in CCHFV is slightly enlarged (Fig. 2b and Supplementary Fig. 3).

These domains collectively organize into a central catalytic cavity that harbors the eight canonical polymerase motifs (A–H) conserved across viral RdRps (Fig. 2c). In the CCHFV L protein, the Palm domain houses catalytic motifs A-E, while the Core lobe and Fingers domain contain motifs G, and F/H, respectively (although motif F was not structurally resolved). Motif A (residues 2346–2367) is essential for catalysis, whereas motif C (residues 2506–2529) contains the invariant aspartate-aspartate residues (D2517 and D2518) and coordinates metal ions for phosphodiester bond formation via interactions involving G2357 (Motif A), D2518 (Motif C), and E2575 (Motif E). Motif B (residues 2474–2489) mediates template recognition and nucleotide binding. Motifs D (residues 2560–2572), E (residues 2573–2583), G (residues 1523–1533), and H (residues 2399–2402)—along with the unresolved motif F (residues 2272–2281)—further stabilize the catalytic center and help form the RNA exit tunnel. Although the Thumb domain lacks conserved catalytic motifs, it contributes to structural stability and positions the RNA strand.

The substrate-free structure reveals both ordered and flexible elements that are functionally linked to replication and transcription. A well-ordered loop (residues 2306–2314) occupies a spatial position corresponding to the Prime-and-Realign (PR) loop (residues 2307–2316) (Fig. 2c), which is essential for replication initiation in LACV[28] and HTNV[23] polymerases. Conversely, the functionally critical priming loop (residues 2838–2860) and the Arch subdomain—implicated in early RNA synthesis and promoter binding, respectively—were not resolved, consistent with their expected conformational flexibility in the absence of RNA substrate. The vRBL and Fingers domains are also incompletely modeled, lacking several regions in the substrate-free state. Additionally, a region absent from the density map (residues 1901–2222) is predicted to fold into a compact domain positioned above the core, similar to the pendant domain observed in the MACV L protein[19].

Collectively, despite substantial variation in full-length sequence and auxiliary domains among *Bunyavirales* RNA polymerases, the catalytic core regions and essential functional motifs are remarkably conserved in both fold topology and spatial arrangement. This structural conservation underscores the catalytic core elucidated here as a critical and common framework for RNA synthesis across the *Bunyavirales* order.

The cryo-EM density map of the CCHFV L protein in the apo state unambiguously reveals four bound metal ions—two zinc (Zn^{2+}) and two manganese (Mn^{2+}) ions—with surrounding residues exhibiting ideal coordination geometry for each metal type (Fig. 2d). The first zinc ion (Zn1) is coordinated by a zinc-finger motif within the vRBL region (C1028/C1031/C1062/C1065), stabilizing a three-helix bundle that corresponds to a single α-helix in the LACV polymerase[26]. The second zinc ion (Zn2) localizes to the interface between the vRBL and Thumb domains (coordinated by H1090/C1294/H1365/E2788) and is inferred to contribute to structural integrity. The first manganese ion (Mn1) resides directly within the RdRp catalytic center, coordinated by acidic residues from conserved motifs A, C and E (G2357/D2518/E2575), and is likely involved in the regulation of enzymatic activity. A second manganese ion (Mn2) is positioned at the interface of the Core lobe, Thumb, and thumb ring (coordinated by R1427/E1430/E3081/N3083). To evaluate the functional impact of divalent cations, we performed polymerase extension assays in the presence of Mg^{2+} or Mn^{2+}. We found that Mn^{2+} is essential for CCHFV L catalytic activity and robustly drives RNA synthesis, whereas Mg^{2+} failed to effectively activate the RdRp (Supplementary Fig. 1d). Given this critical requirement, Mn^{2+} was incorporated into all subsequent cryo-EM sample preparation buffer and served as the sole divalent cation in all subsequent polymerase assays.

Structural basis for 5' vRNA promoter recognition

To elucidate the mechanism of viral RNA recognition, we prepared the CCHFV L protein complex by incubating the purified protein with chemically synthesized 5' vRNA fragments at a molar ratio of 1:1.2. Cryo-EM single-particle analysis yielded a reconstruction at an overall resolution of 2.75 Å, in which the bound 5' vRNA strand was clearly resolved (Fig. 3a, b and Supplementary Fig. 4).

Compared with the apo state structure, the 5' vRNA-bound complex reveals additional well-resolved regions, including the vRBL (residues 1104–1155 and 1171–1220) and Fingers domain (residues 2405–2419 and 2432-2446) (Fig. 3c and Supplementary Fig. 5a–c). The Arch domain (residues 1234–1255), disordered in the apo state, undergoes a clear disorder-to-order transition upon RNA binding (Fig. 3a–c and Supplementary Fig. 5a, b)—a conformational change also observed in HTNV[23] and TSWV[33]. Structural superposition with

the apo structure shows a subtle expansion of the polymerase scaffold (Supplementary Fig. 5d), indicating a slight conformational opening induced by 5' vRNA engagement, with no other large-scale rearrangements observed.

In the CCHFV L–vRNA complex, the first 11 nucleotides of the 5' vRNA promoter are clearly resolved (Fig. 3b). The RNA adopts the characteristic hook-like conformation similar among *Bunyavirales* 5' vRNA promoters[22,23,26], with its architecture stabilized primarily by a canonical Watson–Crick base pair between C2 and G8 (Fig. 3b). The single-base-pair configuration resembles those observed in SFTSV and LASV RNA polymerases[22,31], but differs from the two-base-pair architectures found in HTNV (G3–C11 and U4–A10) and TSWV (G2–C9 and A3–U8)[23,33]. The 5' vRNA binds within a cleft formed by the Fingers, vRBL, Core lobe and Arch domains (Fig. 3a, c). This binding pocket exhibits a strong positive electrostatic potential, complementary to the RNA backbone (Fig. 3d and Supplementary Fig 5e). The hook-binding cleft formed by these domains is structurally conserved in other bunyaviral polymerases—including HTNV, LASV and LACV (Supplementary Fig. 5f)—indicating that this architecture mediating 5' vRNA promoter recognition represents a conserved and essential feature for replication initiation across the *Bunyavirales* order.

The 5' vRNA is anchored within the binding pocket through an extensive and specific network of non-covalent interactions (Fig. 3e, f). Its phosphate backbone is coordinated by salt bridges and hydrogen bonds involving residues from multiple domains: N1077 and K1080 (vRBL), R1252 (Arch), K1261, E1380, Q1517, S1549, R1551, R1552 and N2413 (Core lobe), and N2447 (Fingers). The RNA bases and ribose sugars are further stabilized by hydrogen bonds with S1073, N1381 and Y1399 (vRBL); R1257, N1259 and D1260 (Core lobe); S1248, R1252 and F1255 (Arch); and S2407, K2410, S2443 and N2447 (Fingers). Additionally, three key cation–π interactions lock the RNA in place: R1252 with nucleobase G8, R1257 with A5, and R1551 with C4. This intricate interaction network illustrates how electrostatic, hydrogen-bonding, and aromatic interactions act cooperatively to achieve precise, high-affinity promoter docking.

Although 5' vRNA binding stabilizes the adjacent regions—including the Fingers, vRBL, and Arch domains—the catalytic motif F and the priming loop remain unresolved. In most bunyaviral RNA polymerases, these elements become ordered upon 5' vRNA binding,

priming the enzyme for initiation[23,26,33]. Their absence in the CCHFV L-5' vRNA complex points to a more stringent, checkpoint-like activation mechanism. Thus, 5' vRNA binding induces structural organization of the vRBL arch, creating a scaffold for subsequent 3' vRNA recruitment, but is insufficient to fully assemble the active centre. We propose that structural ordering of motif F and the priming loop is contingent upon the entry and correct positioning of the 3' vRNA template, indicating a stepwise process for polymerase activation.

Identification of suramin as a CCHFV RNA polymerase inhibitor

To identify antiviral inhibitors of the CCHFV RNA polymerase, we first evaluated a panel of compounds including established nucleoside analogues—favipiravir (T-705), ribavirin, obeldesivir, and 2'-deoxy-2'-fluorocytidine (2'-FdC) (Supplementary Fig. 6a–d)[34-38]. We also included suramin (Fig. 4a), given its reported activity against the RNA polymerases of several negative-strand RNA viruses (such as Ebola virus[39]) and other viral families (coronaviruses[40] and norovirus[41]), as well as its documented effects against other *Bunyavirales* members (notably SFTSV and RVFV, albeit through binding to the nucleoprotein[42,43]). Compound effects were assessed using two criteria: binding affinity to the CCHFV L protein measured by surface plasmon resonance (SPR), and dose-dependent inhibition of enzymatic activity determined by primer-extension assays.

Suramin exhibited appreciable affinity for the CCHFV L protein (K_D = 18.4 μM) (Fig. 4b). Dose-response enzymatic assays demonstrated that suramin inhibits polymerase activity in a concentration-dependent manner, with complete inhibition achieved at concentrations between 3.9 and 7.8 μM (Fig. 4c). Conversely, SPR detected no measurable binding for any of the nucleoside analogues tested (Supplementary Fig. 6e–h), and none showed significant inhibition in enzymatic assays (Fig. 4d). Based on these results, we proceeded to structural studies to elucidate the mechanism of suramin-mediated inhibition.

Cryo-EM structure of the CCHFV RNA polymerase in complex with suramin

The CCHFV L–suramin complex was prepared by incubating the L protein with 0.1 mM suramin for 30 min. Cryo-EM analysis of the complex yielded a reconstruction at a global

resolution of 2.5 Å (Supplementary Fig. 7). Unexpectedly, the density map revealed two spatially distinct binding sites (Fig. 5a), each occupied by multiple suramin molecules: site 1 binds two molecules, whereas site 2 binds three (Fig. 5b, c). This unusual dual-site, multi-ligand occupancy suggests a previously unrecognized mechanism of polymerase inhibition.

At the first binding site (Suramin$^{1\#}$), two suramin molecules (designated Suramin^{1A} and Suramin^{1B}, respectively) were identified, each partially resolved and modeled as a fragment comprising two naphthalene and two benzene rings (Fig. 5c). The two partially resolved suramin molecules associate tightly through three π–π stacking interactions between their naphthalene and benzene rings, stabilized by two hydrogen-bonding pairs (Supplementary Fig. 8a, b). As a dimeric unit, they interact with the polymerase via an extensive interface (Fig. 5d and Supplementary Fig. 8c): cation–π interactions between K1379 and a benzene ring (ring D) of Suramin^{1A}, and between R1552 and its naphthalene ring (ring D); multiple hydrogen bonds and salt bridges involving residues K1379, Q1404, R1403, S1515, Q1516, Q1517, S1549, R1551, and R1552 with Suramin^{1A} and a single hydrogen bond anchoring Y1399 to a sulfonate group on the naphthalene ring (ring B) of Suramin^{1B}.

At the second binding site (Suramin$^{2\#}$), three suramin molecules (Suramin^{2A}, Suramin^{2B}, and Suramin^{2C}) form a stable assembly (Fig. 5c). Among these, Suramin^{2A} is fully resolved, whereas Suramin^{2B} is modeled with two naphthalene rings and three benzene rings (rings A-D and D'), and Suramin^{2C} comprises the central four benzene rings (rings C/D/C'/D') (Supplementary Fig. 8b). This assembly is stabilized by an extensive network consisting of ten π–π stacking interactions and ten hydrogen bonds—four between sulfonate groups and amide/urea linkages, and six among amide/urea linkages themselves (Supplementary Fig. 8b). This assembly engages the polymerase through a multifaceted interface (Fig. 5e and Supplementary Fig. 8d). Three cation–π interactions link R1671 to ring D of Suramin^{2A} and ring C of Suramin^{2C}, and R1659 to ring C' of Suramin^{2A}. For Suramin^{2A}, hydrogen bonds and salt bridges connect K1565 and Q1768 to the sulfonate on ring A, and residues A1673, K1672, N1669, and S1761 to the sulfonate on ring A'. Additionally, R1662 and R1659 hydrogen-bond to the carbonyl oxygen between rings C' and D', and K1655 hydrogen-bonds with the central urea oxygen. Suramin^{2B} is anchored by five hydrogen bonds or salt

bridges involving S957 and K1655 with its naphthalene sulfonate, and a hydrogen bond from R1671 to the oxygen of the amide bond between B-C rings. Finally, a van der Waals contact occurs between A1673 and ring D of Suramin[2C].

Unique dual-site inhibitory mechanism on CCHFV polymerase

At the first site, the suramin dimer occupies the positively charged cleft that normally accommodates the 5' vRNA promoter (Fig. 6a). The sulfonate groups of suramin electrostatically mimic the RNA phosphate backbone, engaging the pocket through an extensive interaction network (>15 hydrogen bonds/electrostatic pairs and two cation–π stacks) (Fig. 5d and Supplementary Fig. 8c). Crucially, this recognition involves residues R1252, Y1399, Q1517, S1549, and R1551 (Supplementary Fig. 9a), which are also key determinants for 5' vRNA binding. Unlike viral RNA, suramin at this site contacts only the Core lobe and Fingers subdomains (Fig. 6a); the vRBL and Arch are not involved, with the Arch remaining disordered. Nevertheless, suramin stabilizes the overall fold of the L protein similarly to 5' vRNA: regions of the vRBL and Fingers that are disordered in the apo state become well ordered upon suramin binding (Fig. 5a, b, 6a). Comparison of the apo, RNA-bound, and suramin-bound states shows that suramin induces a subtle contraction around site 1, whereas RNA binding promotes slight expansion—likely reflecting the smaller volume of the suramin dimer relative to the 5' vRNA hook (Supplementary Fig. 9b). Locally, suramin binding also remodels a loop (residues 1373-1380) directed toward the drug (Fig. 6a and Supplementary Fig. 9b). This rearrangement is driven primarily by Lys1379, which undergoes a pronounced conformational shift to form a cation–π interaction with Suramin[1A] (Supplementary Fig. 9a).

Notably, suramin achieves this potent inhibition while engaging fewer structural domains than the vRNA, suggesting a highly efficient mode of steric blockade. Bio-layer interferometry (BLI) revealed that while the 5' vRNA binds the L protein with high affinity and negligible dissociation, pre-incubation with suramin effectively abolishes this interaction (Fig. 6b), demonstrating the potent competitive binding capacity of the inhibitor.

The second site lies on the exterior surface at the Linker–Fingers interface (Fig. 6c), where a positively charged patch facilitates engagement of the negatively charged

suramin assembly (Fig. 6d). The interface is stabilized by 18 hydrogen bonds/salt bridges and three cation–π interactions (Fig. 5e and Supplementary Fig. 8d). Mechanistically, suramin binding stabilizes residues K1672 and A1673 while inducing a forward shift of R1671 and the inward folding of the adjacent loop (residues 1652–1657)—a conformational rearrangement driven by interactions between K1655 and K1656 and the suramin sulfonate groups (Fig. 6e and Supplementary Fig. 9c). Given the role of the Fingers domain in template translocation, suramin likely functions here as a “molecular glue”, allosterically inhibiting enzymatic activity by restricting the domain’s essential conformational plasticity.

Suramin inhibits several viral RNA polymerases, including those of EBOV, SARS-CoV-2, and norovirus, via distinct structural mechanisms. Specifically, it blocks the NTP entry channel to physically prevent substrate access in EBOV[39], occupies the catalytic chamber to impede both template and primer binding in SARS-CoV-2[40], and binds within the Fingers–Thumb cleft to prevent RNA template positioning for initiation in norovirus[41] (Supplementary Fig. 10). In contrast to these established modes of inhibition, our study reveals a unique dual-site mechanism for the CCHFV L protein. Site 1 competitively blocks the 5' vRNA template channel, whereas site 2—distal to the catalytic core—restricts dynamic motions between the Linker and Fingers domains, which are critical for the polymerase cycle. This mode of action resembles the conformational-locking strategy employed by arenaviral Z proteins such as MACV[20,21]. Thus, suramin inhibits CCHFV RNA polymerase through a cooperative two-pronged mechanism: competitive occlusion of the RNA template channel and allosteric locking of inter-domain dynamics. This previously uncharacterized dual-action strategy will open new avenues for designing multi-site inhibitors targeting the CCHFV RNA polymerase.

Binding and inhibition of the CCHFV L protein by suramin derivatives

Although suramin exhibits potent inhibition of CCHFV L protein activity *in vitro*, its unfavorable pharmacokinetic profile limits clinical applicability. To assess its potential as an optimizable scaffold, we evaluated a panel of existing suramin derivatives—NF023, NF157, NF449, and NF546 (Fig. 7a)—for binding affinity and inhibitory activity against the viral RdRp. SPR assays showed that NF023 and NF546 bound with affinities (K_D = 18.0 μM

and 17.5 μM, respectively) similar to suramin (K_D = 18.4 μM), whereas NF157 showed slightly weaker affinity (K_D= 25.2 μM, ~1.4-fold lower) and NF449 exhibited stronger binding (K_D = 7.6 μM, ~2.4-fold higher) (Fig. 7b–e). In enzymatic assays (Fig. 7f–i), however, NF449—despite its enhanced affinity—displayed reduced inhibition compared to suramin, whereas NF157 exhibited potency comparable to the parent compound. NF023 and NF546 showed diminished inhibitory effects.

These results demonstrate suramin-based analogues retain the ability to bind and inhibit the CCHFV L protein, likely through conserved structural interactions. The observed discordance between binding affinity and inhibitory efficacy—exemplified by NF157 and NF449—highlights the need to balance these properties in future optimization efforts. Structural studies of suramin derivatives in complex with the polymerase will be helpful to elucidate the mechanistic basis of these discrepancies and guide rational optimization. Together, these findings support the suramin scaffold as a viable starting point for developing drug-like inhibitors against CCHFV and related bunyaviruses.

Discussion

Here, we present high-resolution cryo-EM structures of the CCHFV RNA polymerase catalytic core in three functional states—apo, 5' vRNA-bound, and in complex with the non-nucleotide inhibitor suramin. These structures elucidate the architecture of the polymerase core, the structural basis for viral RNA promoter recognition, and the mechanism of inhibition. Comparative analysis with other bunyaviral polymerases shows that the core region of the CCHFV L protein adopts the canonical fold conserved across the *Bunyavirales* family. Key subdomains—including the catalytic Palm and Thumb, the conserved motifs forming the active site, and the 5' vRNA-binding pocket—exhibit high structural similarity. This shared architecture indicates that CCHFV RNA polymerase operates within a conserved catalytic framework, employing an evolutionarily conserved mechanism for RNA transcription and replication that is fundamental to the entire *Bunyavirales* family.

Building on the structural information obtained in this study and homology modeling of *Bunyavirales* counterparts, we propose a dynamic structural model of the CCHFV replication cycle (Fig. 8a, b and Supplementary Fig. 11). This model delineates the

sequential conformational states of the polymerase core—transitioning from the resting state to pre-initiation complex assembly and the elongation phase of RNA synthesis. By explicitly mapping the pathways for template and NTP entry, as well as the exit channels for the template and product RNA relative to the active site, we provide a comprehensive framework for understanding the orchestrated replication mechanism of the CCHFV polymerase.

Therapeutic targeting of the Bunyavirales polymerase remains significant challenge, and to date, no specific antiviral therapies are approved for CCHFV. Existing research has predominantly focused on nucleoside analogs, including ribavirin, favipiravir, and 4'-fluorocytidine (4'-FlC)[44]. Although ribavirin is employed clinically, evidence for its ability to reduce mortality is insufficient, rendering its efficacy as a monotherapy uncertain[45,46]. Similarly, while favipiravir inhibits the viral polymerase and exhibits antiviral activity against CCHFV and other viruses in cellular and animal models, its therapeutic benefit in humans remains unproven[6,47-49]. In contrast, non-nucleoside inhibitors (NNIs) function not by incorporation into the RNA chain but by binding to distinct sites on the RdRp to abrogate enzymatic activity, thus offering a mechanistic strategy complementary to nucleoside analogs. Here, we demonstrate that suramin—a century-old pharmaceutical[50]—significantly inhibits the CCHFV L protein *in vitro*, revealing a potent antiviral profile with a distinct mechanism of action.

Our structural and functional analyses establish that suramin inhibits CCHFV RNA polymerase through a unique dual-site synergistic mechanism (Fig. 8c). First, it acts as a competitive inhibitor by occupying the 5' vRNA-binding site, thereby blocking template loading and replication initiation. Second, it functions as a “molecular glue” at the Finger-Linker interface, likely locking the polymerase in a conformation that restricts the structural dynamics essential for elongation. This dual-site targeting offers several advantages: (1) simultaneous disruption of both initiation and elongation creates a broad antiviral effect, minimizing the potential for viral evasion. (2) the requirement for concurrent mutations at two conserved sites presents a high genetic barrier to resistance, making viral escape evolutionarily less probable than with single-target inhibitors.

The dual-site inhibition of CCHFV by suramin parallels the mechanism recently reported for ribavirin against TSWV[33]. Ribavirin similarly employs a two-pronged strategy:

it targets the 5' vRNA hook-binding site—analogous to suramin at site 1—to disrupt promoter recognition, while simultaneously interfering with the rearrangement of Motif F to prevent catalytic core assembly. This mechanistic convergence identifies the 5' vRNA hook-binding pocket as an attractive broad-spectrum drug target and establishes dual-site inhibition as a novel and potent paradigm for antiviral design.

Although suramin itself exhibits poor drug-like properties—including high molecular weight and unfavorable pharmacokinetics—it serves as a valuable chemical scaffold. Our work establishes a foundation for developing suramin-based inhibitors with improved pharmaceutical properties. Several available suramin analogs effectively suppress CCHFV L protein polymerase activity, highlighting the potential for optimizing derivatives with improved binding affinity, membrane permeability, and metabolic stability. The dual-site binding mode supports the rational design of smaller, pharmaceutically optimized compounds targeting both pockets. Notably, the primary suramin binding site—which competitively occupies the 5' vRNA-binding pocket—is highly similar across the *Bunyavirales* order (which includes several other highly pathogenic viruses). Consequently, this site represents a critical target for the development of broad-spectrum inhibitors. Meanwhile, the “molecular glue” mechanism observed at the secondary site offers a promising strategy for designing viral-specific inhibitors with potentially reduced host toxicity. Collectively, these structural insights into suramin’s dual-site inhibition mechanism provide a new framework for developing potent and broad-spectrum antivirals against bunyaviruses.

While our structures provide mechanistic insights into the core catalytic region of the CCHFV RNA polymerase, they encompass only approximately half of the full-length protein. The architecture and functional roles of the remaining segments—particularly the flexible N- and C-terminal regions—remain uncharacterized. Future efforts should aim to determine the structures of the full-length CCHFV L protein in additional functional states and in complex with other antiviral candidates. These studies will be critical for systematically elucidating the distinctive catalytic mechanism of CCHFV RNA polymerase and for defining the diverse modes of action of prospective antiviral therapies.

Materials and methods

Protein expression and purification

The gene encoding the full-length Crimean–Congo hemorrhagic fever virus (CCHFV) L protein (UniProt: Q6TQR6) was codon-optimized for mammalian cell expression, synthesized, and cloned into the pCAGGS vector with a C-terminal twin-Strep tag. The endonuclease mutant (K835A/D839A/K842A) was generated by site-directed mutagenesis to abolish its cleavage activity for use in *in vitro* RNA polymerase activity assays. Its expression and purification followed the same procedures as described for the wild-type protein. For protein expression, HEK293F (Invitrogen) cells were seeded at a density of 0.8 × 10^6 cells per ml, which were maintained in SMM 293-TII medium (Sino Biological) at 37 °C with 5% CO_2 in an orbital shaking incubator at 120 rpm. A total of 1 mg plasmid and 3 mg polyethylenimine (PEI; Yeasen) were incubated in 50 ml fresh medium for 20 min before addition to 1 litre of culture. After 24 h, sodium butyrate was added to a final concentration of 5 mM, and cells were incubated for a further 48 h before harvesting by centrifugation (2,500 × *g*, 15 min). Cell pellets were resuspended in Lysis Buffer (50 mM Tris-HCl, pH 8.0, 500 mM NaCl, 5% glycerol, 1mM TCEP) supplemented with cOmplete EDTA-free Protease Inhibitor Cocktail (Roche) and lysed by sonication on ice, and the lysate was clarified by centrifugation (22,000 × *g*, 45 min, 4 °C). The supernatant was incubated with Strep-Tactin XT 4Flow resin (IBA Lifesciences) for 60 min at 4 °C. The resin was washed extensively with Wash Buffer (50 mM Tris-HCl, pH 8.0, 500 mM NaCl, 5% glycerol, 1 mM TCEP, 1 mM EDTA), and target protein was eluted in the same buffer containing 50 mM D-biotin. The eluted protein was concentrated (AmiconUltra, 100 kDa molecular mass cut-off, Millipore) and further purified by size-exclusion chromatography (SEC) on a Superose 6 Increase 10/300 GL column (Cytiva) equilibrated in Lysis Buffer. Fractions containing the target protein were pooled, concentrated to 2–3 mg ml^{-1}, flash-frozen as aliquots in liquid nitrogen, and stored at −80 °C for subsequent biochemical assays. Freshly purified samples were immediately used for cryo-EM sample preparation. Samples from each purification step were analyzed by SDS–PAGE (Supplementary Fig. 1), and protein concentration measured by the absorbance at 280 nm using a NanoDrop spectrophotometer (Thermo Fisher Scientific).

Cryo-EM grid preparation and data collection

Cryo-EM grids were prepared at 4 °C and 100% humidity using a Vitrobot Mark IV (Thermo Fisher Scientific). A 3 µL aliquot of each sample at a final concentration of 0.7 mg mL^{-1} was applied to a freshly glow-discharged Quantifoil R1.2/1.3 300-mesh gold grid. The apo CCHFV L sample was used directly. For the CCHFV L–suramin complex, the protein was pre-incubated with 0.1 mM suramin for at least 30 min on ice before grid application. For the CCHFV L–5' vRNA complex, purified L protein was incubated with 15-nt 5' vRNA promoter at a molar ratio of 1:1.2 for 10 min on ice immediately before freezing to prevent RNA degradation. After 10 s of incubation, excess solution was blotted for 3 s (blot force 2) and the grid was plunge-frozen in liquid ethane. Prepared grids were loaded onto a 300 kV Titan Krios microscope (Thermo Fisher Scientific) equipped with a Falcon 4 direct electron detector (Thermo Fisher Scientific). Movies were automatically collected using EPU software (Thermo Fisher Scientific) in super-resolution mode at a nominal magnification of ×165,000 (calibrated pixel size = 0.73 Å), with a defocus range of -0.8 to -2.5 µm. Each movie was exposed for 3.4 s with a total exposure dose of ~50 e^{-} $Å^{-2}$. Final datasets consisted of 7,939 (apo CCHFV L protein), 4,848 (CCHFV L–5' vRNA complex) and 5,547 (CCHFV L–suramin complex) micrographs.

Cryo-EM data processing

All cryo-EM data processing was performed using cryoSPARC v4.7.0[51]. Beam-induced motion was corrected using Patch Motion Correction, and contrast transfer function (CTF) parameters were estimated via Patch CTF Estimation.

For the apo CCHFV L dataset, a total of 3,444,016 particles were automatically picked from 7,939 micrographs. After two rounds of 2D classification, 196,081 particles displaying distinct structural features were selected for *ab initio* reconstruction (using five classes) and subsequent heterogeneous refinement. A homogeneous subset of 48,496 particles exhibiting well-defined density was then subjected to local CTF refinement and non-uniform refinement, yielding a final map at a global resolution of 2.59 Å resolution.

For the CCHFV L–suramin complex, 1,056,252 and 3,018,770 particles were initially picked from 5,547 micrographs using the Blob picker and Template picker, respectively. Following two rounds of 2D classification, 193,360 and 232,391 particles were retained from the respective subsets. After merging and removing duplicate particles using a threshold distance of 0.4 times the particle diameter, the resulting stack was used for *ab initio* reconstruction and 3D classification. The final set of 37,822 particles underwent reference-based motion correction and non-uniform refinement, resulting in a map with a global resolution of 2.5 Å.

For the CCHFV L–5' vRNA complex, 1,681,455 and 4,033,305 particles were picked from 4,848 micrographs using Blob picker and Template picker, respectively. Subsequent processing followed the same workflow as the L–suramin complex. A final reconstruction with a global resolution of 2.75 Å was obtained from 66,103 particles.

Global resolution was determined using the gold-standard Fourier shell correlation (FSC) criterion of 0.143. Local resolution was estimated in cryoSPARC. Detailed processing workflows and data collection statistics are summarized in Supplementary Figs. 1, 4, and 7 and Supplementary Table 1.

Atomic model building

Model building was initiated with the CCHFV L–5' vRNA complex. An initial atomic model was generated by segmenting the AlphaFold-predicted model into individual domains and docking them into the cryo-EM density map using UCSF ChimeraX[52]. The model was then subjected to iterative cycles of manual adjustment in Coot[53] and real-space refinement in PHENIX[54] until the model parameters converged, and model geometry and fit met standard validation criteria (including MolProbity score, rotamer and Ramachandran outliers). The models for the apo CCHFV L and the CCHFV L–suramin complex were obtained by rigid-body docking of the refined L–5' vRNA model into their respective cryo-EM maps in UCSF ChimeraX, followed by manual adjustment in Coot. These models subsequently underwent the same iterative refinement protocol as described above. Model statistics are summarized in Supplementary Table 1. Structural analysis, model building, and figure preparation were performed using Coot, UCSF ChimeraX and PyMOL (https://pymol.org/).

In vitro RNA polymerase activity assay

To reconstitute the functional viral promoter, RNA oligonucleotides corresponding to the CCHFV genomic termini were chemically synthesized. The 26-nt 3' vRNA strand was hybridized with 15-nt 5' vRNA primer/hook strands at a 1:1.5 molar ratio in annealing buffer (50 mM Tris-HCl, pH 8.0, 150 mM NaCl) by heating to 90 °C for 2 min , followed by gradual cooling to 4 °C over 2 h. Polymerase reactions (10 µL final volume) were carried out in reaction buffer (50 mM Tris-HCl, pH 8.0, 150 mM NaCl, 1 mM DTT, 5% (v/v) glycerol, and 5 mM $MnCl_2$). For divalent cation dependence experiments, $MnCl_2$ was substituted with 5 mM $MgCl_2$ where indicated. Purified CCHFV L protein (0.5 µM) was pre-incubated with 200 nM of the annealed RNA promoter for 10 min on ice. Reactions were initiated by the addition of NTPs to a final concentration of 1 mM each and incubated at 30 °C for 2 h. Reactions were terminated by adding an equal volume of stop buffer (20 mM EDTA, 0.01% bromophenol blue, 0.01% xylene cyanol) and heating at 95 °C for 5 min. Extension products were separated on a 15% denaturing urea–polyacrylamide gel (7 M urea) at 180 V for 80 min and visualized using a ChemiDoc MP Imaging System (Bio-Rad). All assays were independently repeated at least three times.

RNA sequences used:

3' vRNA (26-nt): 5'–GUGUGGGGGGAACGAUUUCUUUGAGA–3'

5' vRNA (15-nt): 5'–FAM-UCUCAAAGAAAUCGU–3'

Surface plasmon resonance (SPR) assay

Binding affinities between CCHFV L protein and small-molecule inhibitors—including five non-nucleotide analogues (suramin, NF023, NF157, NF449, NF546) and four nucleotide analogues (favipiravir, ribavirin, obeldesivir, 2'-deoxy-2'-fluorocytidine)—were measured by surface plasmon resonance using a Biacore 8K+ system (Cytiva) at 25 °C. The CCHFV L protein was covalently immobilized on a Series S CM5 sensor chip via amine coupling in 10 mM sodium acetate (pH 4.5), followed by quenching with 1 M ethanolamine. Analytes were serially diluted (0.156–20 µM) in PBS buffer containing 0.05% Tween 20, and injected at a flow rate of 30 µL/min. Each cycle comprised an 80 s association phase and an 80 s

dissociation phase. No regeneration was required between cycles due to complete analyte dissociation. Sensorgram data were double-referenced and analyzed using Biacore Insight Evaluation Software. Kinetic constants were obtained by fitting to a 1:1 binding model; for compounds exhibiting rapid kinetics, the equilibrium dissociation constants (K_D) were determined by steady-state affinity analysis. All assays were independently repeated at least three times.

Bio-layer interferometry (BLI) assay

Binding kinetics between CCHFV L protein and RNA, as well as suramin inhibition, were analyzed by bio-layer interferometry on an Octet Red 384 system (Sartorius) at 25 °C with shaking at 1,000 rpm. Streptavidin (SA) biosensors (Sartorius, Cat. # 18-5019) were equilibrated in kinetics buffer (50 mM Tris-HCl, pH 8.0, 100 mM NaCl, 0.05% Tween-20) for 10 min. Biotinylated 5' vRNA (200 nM) was loaded onto the sensors for 90 s, followed by a 60 s baseline equilibration. For binding kinetics, sensors were incubated with serially diluted CCHFV L protein at concentrations ranging from 200 nM to 3.125 nM (two-fold serial dilutions) for 600 s (association) and then transferred to kinetics buffer for 600 s (dissociation). For inhibition assays, the same protein dilution series was pre-incubated with 10 μM suramin for 30 min prior to measurement. Parallel reference wells containing immobilized RNA exposed only to 10 μM suramin were used to correct for system drift and non-specific binding. All data were globally fitted to a 1:1 binding model using Octet Analysis Studio software to determine binding affinities and inhibitory potency. All assays were independently repeated at least three times.

Data availability

The cryo-EM density maps and corresponding atomic coordinates have been deposited in the Electron Microscopy Data Bank (EMDB) and Protein Data Bank (PDB), respectively, under accession codes PDB 22TE, EMD-68655 (CCHFV L protein alone), PDB 22TR, EMD-68663 (CCHFV L–5' vRNA complex), PDB 22TH, EMD-68657 (CCHFV L–suramin complex). All other data supporting the findings of this study are available from the

corresponding author upon reasonable request. Source data are provided with this paper.

Acknowledgements

Cryo-EM data collection was performed at the Structural Biology Core Facility of Shenzhen Medical Academy of Research and Translation (SMART). We are grateful to Dr. Gang Fu for assistance with TEM maintenance, cryo-EM sample screening, and data collection. We thank the Sample Preparation and Analysis Core Facility of the Bio-Tech Center of SMART for technical support for SPR and BLI analysis. This work was supported by grants from the Shenzhen Bay Laboratory Startup Fund (21330061) to J.M.

Author contributions

J. M. conceived and supervised the project, and designed all the experiments. K.Y., H.W. and X.L. performed protein purification and biochemical assays. H.W., X.L. and J.Z. prepared and screened cryo-EM specimens. H.W., Z.L. and J.Z. collected and processed cryo-EM data and built the atomic models. Y.W. supervised the experiments and reviewed the manuscript. J.M. wrote the manuscript with assistance from K.Y. All authors contributed to data analysis, discussed the results and approved the final manuscript.

Competing interests

The authors declare no competing interests.

References

1 McFadden, E. *et al.* Engineering and structures of Crimean-Congo hemorrhagic fever virus glycoprotein complexes. *Cell* **188**, 303–315 e313 (2025). https://doi.org/10.1016/j.cell.2024.11.008

2 Ritter, M. *et al.* The low-density lipoprotein receptor and apolipoprotein E associated with CCHFV particles mediate CCHFV entry into cells. *Nat Commun* **15**, 4542 (2024). https://doi.org/10.1038/s41467-024-48989-5

3 Monteil, V. M. *et al.* Crimean-Congo haemorrhagic fever virus uses LDLR to bind and enter host cells. *Nat Microbiol* **9**, 1499–1512 (2024). https://doi.org/10.1038/s41564-024-01672-3

4 Golden, J. W. *et al.* GP38-targeting monoclonal antibodies protect adult mice against lethal Crimean-Congo hemorrhagic fever virus infection. *Sci Adv* **5**, eaaw9535 (2019). https://doi.org/10.1126/sciadv.aaw9535

5 Hawman, D. W. & Feldmann, H. Crimean-Congo haemorrhagic fever virus. *Nat Rev Microbiol* **21**, 463–477 (2023). https://doi.org/10.1038/s41579-023-00871-9

6 Frank, M. G. *et al.* Crimean-Congo Hemorrhagic Fever Virus for Clinicians-Diagnosis, Clinical Management, and Therapeutics. *Emerg Infect Dis* **30**, 864–873 (2024). https://doi.org/10.3201/eid3005.231648

7 Bente, D. A. *et al.* Crimean-Congo hemorrhagic fever: history, epidemiology, pathogenesis, clinical syndrome and genetic diversity. *Antiviral Res* **100**, 159–189 (2013). https://doi.org/10.1016/j.antiviral.2013.07.006

8 WHO. (World Health Organization Geneva, Switzerland, 2018).

9 Ma, J. *et al.* Identification of a new orthonairovirus associated with human febrile illness in China. *Nat Med* **27**, 434–439 (2021). https://doi.org/10.1038/s41591-020-01228-y

10 Zhang, X. A. *et al.* A New Orthonairovirus Associated with Human Febrile Illness. *N Engl J Med* **391**, 821–831 (2024). https://doi.org/10.1056/NEJMoa2313722

11 Zhang, M. Z. *et al.* Human Infection with a Novel Tickborne Orthonairovirus Species in China. *N Engl J Med* **392**, 200–202 (2025). https://doi.org/10.1056/NEJMc2410853

12 Iglesias-Rivas, P., Gonzalez-Vazquez, L. D. & Arenas, M. Molecular Evolution and Phylogeography of the Crimean-Congo Hemorrhagic Fever Virus. *Viruses* **17** (2025). https://doi.org/10.3390/v17081054

13 Zivcec, M., Scholte, F. E., Spiropoulou, C. F., Spengler, J. R. & Bergeron, E. Molecular Insights into Crimean-Congo Hemorrhagic Fever Virus. *Viruses* **8**, 106 (2016). https://doi.org/10.3390/v8040106

14 Kuang, W. *et al.* Structure and function of the nairovirus cap-snatching endonuclease. *Nucleic Acids Res* **54** (2026). https://doi.org/10.1093/nar/gkaf1515

15 Leventhal, S. S. *et al.* Antibodies targeting the Crimean-Congo Hemorrhagic Fever Virus nucleoprotein protect via TRIM21. *Nat Commun* **15**, 9236 (2024). https://doi.org/10.1038/s41467-024-53362-7

16 Akutsu, M., Ye, Y., Virdee, S., Chin, J. W. & Komander, D. Molecular basis for ubiquitin and ISG15 cross-reactivity in viral ovarian tumor domains. *Proc Natl Acad Sci U S A* **108**, 2228–2233 (2011). https://doi.org/10.1073/pnas.1015287108

17 Spengler, J. R. *et al.* RIG-I Mediates an Antiviral Response to Crimean-Congo Hemorrhagic Fever Virus. *J Virol* **89**, 10219–10229 (2015). https://doi.org/10.1128/JVI.01643-15

18 Scholte, F. E. M. *et al.* Crimean-Congo Hemorrhagic Fever Virus Suppresses Innate Immune Responses via a Ubiquitin and ISG15 Specific Protease. *Cell Rep* **20**, 2396–2407 (2017). https://doi.org/10.1016/j.celrep.2017.08.040

19 Peng, R. *et al.* Structural insight into arenavirus replication machinery. *Nature* **579**, 615–619 (2020). https://doi.org/10.1038/s41586-020-2114-2

20 Xu, X. *et al.* Cryo-EM structures of Lassa and Machupo virus polymerases complexed with cognate regulatory Z proteins identify targets for antivirals. *Nat Microbiol* **6**, 921–931 (2021). https://doi.org/10.1038/s41564-021-00916-w

21 Ma, J., Zhang, S. & Zhang, X. Structure of Machupo virus polymerase in complex with matrix protein Z. *Nat Commun* **12**, 6163 (2021). https://doi.org/10.1038/s41467-021-26432-3

22 Kouba, T. *et al.* Conformational changes in Lassa virus L protein associated with promoter binding and RNA synthesis activity. *Nat Commun* **12**, 7018 (2021). https://doi.org/10.1038/s41467-021-27305-5

23 Durieux Trouilleton, Q., Barata-Garcia, S., Arragain, B., Reguera, J. & Malet, H. Structures of active Hantaan virus polymerase uncover the mechanisms of Hantaviridae genome replication. *Nat Commun* **14**, 2954 (2023). https://doi.org/10.1038/s41467-023-38555-w

24 Durieux Trouilleton, Q., Housset, D., Tarillon, P., Arragain, B. & Malet, H. Structural characterization of the oligomerization of full-length Hantaan virus polymerase into symmetric dimers and hexamers. *Nat Commun* **15**, 2256 (2024). https://doi.org/10.1038/s41467-024-46601-4

25 Keown, J. R., Carrique, L., Nilsson-Payant, B. E., Fodor, E. & Grimes, J. M. Structural characterization of the full-length Hantaan virus polymerase. *PLoS Pathog* **20**, e1012781 (2024). https://doi.org/10.1371/journal.ppat.1012781

26 Gerlach, P., Malet, H., Cusack, S. & Reguera, J. Structural Insights into Bunyavirus Replication and Its Regulation by the vRNA Promoter. *Cell* **161**, 1267–1279 (2015). https://doi.org/10.1016/j.cell.2015.05.006

27 Arragain, B. *et al.* Pre-initiation and elongation structures of full-length La Crosse virus polymerase reveal functionally important conformational changes. *Nat Commun* **11**, 3590 (2020). https://doi.org/10.1038/s41467-020-17349-4

28 Arragain, B. *et al.* Structural snapshots of La Crosse virus polymerase reveal the mechanisms underlying Peribunyaviridae replication and transcription. *Nat Commun* **13**, 902 (2022). https://doi.org/10.1038/s41467-022-28428-z

29 Wang, P. *et al.* Structure of severe fever with thrombocytopenia syndrome virus L protein elucidates the mechanisms of viral transcription initiation. *Nat Microbiol* **5**, 864–871 (2020). https://doi.org/10.1038/s41564-020-0712-2

30 Vogel, D. *et al.* Structural and functional characterization of the severe fever with thrombocytopenia syndrome virus L protein. *Nucleic Acids Res* **48**, 5749–5765 (2020). https://doi.org/10.1093/nar/gkaa253

31 Williams, H. M. *et al.* Structural insights into viral genome replication by the severe fever with thrombocytopenia syndrome virus L protein. *Nucleic Acids Res* **51**, 1424–1442 (2023). https://doi.org/10.1093/nar/gkac1249

32 Wang, X. *et al.* Structure of Rift Valley Fever Virus RNA-Dependent RNA Polymerase. *J Virol* **96**, e0171321 (2022). https://doi.org/10.1128/JVI.01713-21

33 Li, J. *et al.* Structural basis for the activation of plant bunyavirus replication machinery and its dual-targeted inhibition by ribavirin. *Nat Plants* **11**, 518–530 (2025). https://doi.org/10.1038/s41477-025-01940-y

34 Oestereich, L. *et al.* Evaluation of antiviral efficacy of ribavirin, arbidol, and T-705 (favipiravir) in a mouse model for Crimean-Congo hemorrhagic fever. *PLoS Negl Trop Dis* **8**, e2804 (2014). https://doi.org/10.1371/journal.pntd.0002804

35 Tasdelen Fisgin, N., Ergonul, O., Doganci, L. & Tulek, N. The role of ribavirin in the therapy of Crimean-Congo hemorrhagic fever: early use is promising. *Eur J Clin Microbiol Infect Dis* **28**, 929–933 (2009). https://doi.org/10.1007/s10096-009-0728-2

36 Welch, S. R. *et al.* Identification of 2'-deoxy-2'-fluorocytidine as a potent inhibitor of Crimean-Congo hemorrhagic fever virus replication using a recombinant fluorescent reporter virus. *Antiviral Res* **147**, 91–99 (2017). https://doi.org/10.1016/j.antiviral.2017.10.008

37 Pitts, J. *et al.* Oral dosing of the nucleoside analog obeldesivir is efficacious against RSV infection in African green monkeys. *Nat Commun* **16**, 6437 (2025). https://doi.org/10.1038/s41467-025-61595-3

38 Cross, R. W. *et al.* Oral administration of obeldesivir protects nonhuman primates against Sudan ebolavirus. *Science* **383**, eadk6176 (2024). https://doi.org/10.1126/science.adk6176

39 Yuan, B. *et al.* Structure of the Ebola virus polymerase complex. *Nature* **610**, 394–401 (2022). https://doi.org/10.1038/s41586-022-05271-2

40 Yin, W. *et al.* Structural basis for inhibition of the SARS-CoV-2 RNA polymerase by suramin. *Nat Struct Mol Biol* **28**, 319–325 (2021). https://doi.org/10.1038/s41594-021-00570-0

41 Mastrangelo, E. *et al.* Structure-based inhibition of Norovirus RNA-dependent RNA polymerases. *J Mol Biol* **419**, 198–210 (2012). https://doi.org/10.1016/j.jmb.2012.03.008

42 Jiao, L. *et al.* Structure of severe fever with thrombocytopenia syndrome virus nucleocapsid protein in complex with suramin reveals therapeutic potential. *J Virol* **87**, 6829–6839 (2013). https://doi.org/10.1128/JVI.00672-13

43 Ellenbecker, M., Lanchy, J. M. & Lodmell, J. S. Inhibition of Rift Valley fever virus replication and perturbation of nucleocapsid-RNA interactions by suramin. *Antimicrob Agents Chemother* **58**, 7405–7415 (2014). https://doi.org/10.1128/AAC.03595-14

44 Cross, R. W. *et al.* Oral 4'-fluorouridine rescues nonhuman primates from advanced Lassa fever. *Nature* (2026). https://doi.org/10.1038/s41586-025-09906-y

45 Johnson, S. *et al.* Ribavirin for treating Crimean Congo haemorrhagic fever. *Cochrane Database Syst Rev* **6**, CD012713 (2018). https://doi.org/10.1002/14651858.CD012713.pub2

46 Ascioglu, S., Leblebicioglu, H., Vahaboglu, H. & Chan, K. A. Ribavirin for patients with Crimean-Congo haemorrhagic fever: a systematic review and meta-analysis. *J Antimicrob Chemother* **66**, 1215–1222 (2011). https://doi.org/10.1093/jac/dkr136

47 Hawman, D. W. *et al.* Efficacy of favipiravir (T-705) against Crimean-Congo hemorrhagic fever virus infection in cynomolgus macaques. *Antiviral Res* **181**, 104858 (2020). https://doi.org/10.1016/j.antiviral.2020.104858

48 Tipih, T. *et al.* Favipiravir and Ribavirin protect immunocompetent mice from lethal CCHFV infection. *Antiviral Res* **218**, 105703 (2023). https://doi.org/10.1016/j.antiviral.2023.105703

49 Hawman, D. W. *et al.* Favipiravir (T-705) but not ribavirin is effective against two distinct strains of Crimean-Congo hemorrhagic fever virus in mice. *Antiviral Res* **157**, 18–26 (2018). https://doi.org/10.1016/j.antiviral.2018.06.013

50 Brun, R., Blum, J., Chappuis, F. & Burri, C. Human African trypanosomiasis. *Lancet* **375**, 148–159 (2010). https://doi.org/10.1016/S0140-6736(09)60829-1

51 Punjani, A., Rubinstein, J. L., Fleet, D. J. & Brubaker, M. A. cryoSPARC: algorithms for rapid unsupervised cryo-EM structure determination. *Nat Methods* **14**, 290–296 (2017). https://doi.org/10.1038/nmeth.4169

52 Pettersen, E. F. *et al.* UCSF ChimeraX: Structure visualization for researchers, educators, and developers. *Protein Sci* **30**, 70–82 (2021). https://doi.org/10.1002/pro.3943

53 Casanal, A., Lohkamp, B. & Emsley, P. Current developments in Coot for macromolecular model building of Electron Cryo-microscopy and Crystallographic Data. *Protein Sci* **29**, 1069–1078 (2020). https://doi.org/10.1002/pro.3791

54 Afonine, P. V. *et al.* Real-space refinement in PHENIX for cryo-EM and crystallography. *Acta Crystallogr D Struct Biol* **74**, 531–544 (2018). https://doi.org/10.1107/S2059798318006551

Figure Legends

Fig. 1: Cryo-EM structure of the Crimean-Congo hemorrhagic fever virus (CCHFV) L protein. a Domain architecture of the CCHFV L protein. Domain assignments are based on structural conservation among viral RNA polymerases of the order *Bunyavirales*. Domains are colored as follows: Linker (grey), Core lobe (wheat), vRBL (magenta), Arch (smudge), Fingers (orange), Palm (pink), Thumb (slate), Bridge (red), Thumb ring (cyan) and Lid (green). Residue boundaries are indicated above. Solid bars indicate regions resolved by cryo-EM; grey hatched bars represent known functional domains (OTU and endonuclease) that were not resolved. Structurally and functionally uncharacterized regions are shown in white. Regions corresponding to PA, PB1 and PB2 are indicated. **b** Cryo-EM density maps of the apo CCHFV L protein shown in three orthogonal views and colored according to the domain scheme in (**a**). Key structural features are labeled. **c** Cartoon representation of the CCHFV L protein in the same orientations as (**b**), with domains colored accordingly.

Fig. 2: Structure and conservation of the CCHFV L protein. a Structural comparison of the CCHFV L protein (this work) with other polymerases of the order *Bunyavirales*: SFTSV (PDB 8AS7), LACV (PDB 5AMR), HTNV (PDB 8C4T), and LASV (PDB 7OJN). The overall fold is highly conserved across the *Nairovirus*, *Phlebovirus*, *Orthobunyavirus*, *Orthohantavirus*, and *Mammarenavirus* genera. **b** Detailed structural superposition of individual segments (Linker–Fingers, Core lobe, Palm, vRBL, Thumb-Thumb ring-Lid), highlighting the similarity of secondary structural elements. **c** Conservation of key RdRp catalytic motifs and loops. The arrangement of conserved viral RdRp motifs A–H and the Prime-and-Realign (PR) loop is shown; each motif is colored differently with its amino acid range labelled. Motif F and the priming loop were not resolved. Key residues D2517 and D2518 are shown as sticks. **d** Four metal ions identified in the cryo-EM density map, including two zinc (Zn^{2+}) and two (Mn^{2+}) ions. Panels 1 and 2 show two structural Zn^{2+} ions coordinated by C1028/C1031/C1062/C1065 and H1090/C1294/H1365/E2788, respectively. Panels 3 and 4 show two Mn^{2+} ions coordinated by G2357/D2518/E2575 and R1427/E1430/E3081/N3083.

Fig. 3: Recognition of the 5' vRNA hook by the CCHFV L protein. a Overall view of the CCHFV L protein (colored as in **Fig. 1**) in complex with the 5' vRNA (green). Left, cryo-EM density map; right, atomic model in cartoon representation. The RNA binds in a pocket formed by the vRBL, Arch, Fingers, and Core lobe domains. **b** Cryo-EM density map (mesh) and atomic model (sticks) of the 5' vRNA, which adopts a characteristic stem-loop "hook" structure formed by base pairing between nucleotides C2-G8. **c** Close-up view of the 5' vRNA binding pocket. Structural comparison of the 5' vRNA-bound state (left) and the apo state (right) shows that RNA binding induces local conformational stabilisation in the arch, vRBL and fingers domains. **d** Electrostatic potential surface of the RNA-binding cleft showing that the 5' vRNA hook binds into a highly basic cavity. Scale bar is shown. **e** Detailed interaction network recognizing the 5' vRNA. Interacting residues are shown as sticks and labelled; RNA is shown as a cartoon and the protein backbone as a transparent cartoon. **f** Schematic diagram summarizing the intermolecular contacts between L protein residues and the 5' vRNA nucleotides. Hydrogen bonds and salt bridges are indicated by dashed lines; cation–π interactions by double solid lines.

Fig. 4: Suramin is a potent inhibitor of the CCHFV L protein. a Chemical structure of suramin. **b** Surface plasmon resonance (SPR) analysis of suramin binding to the CCHFV L protein. Left, sensorgrams showing binding at increasing concentrations (0.1563–20 μM). Right, steady-state affinity fitting yielding a dissociation constant (K_D) of 18.4 μM. **c** *In vitro* polymerase activity assay showing dose-dependent inhibition of RNA synthesis by suramin. The production of RNA products longer than 28 nt decreases with increasing suramin concentration. **d** *In vitro* polymerase activity assay of nucleotide analogues against the CCHFV L protein. Activity is not inhibited by favipiravir, ribavirin, 2'-FdC or obeldesivir at concentrations up to 1 mM. Data are representative of $n = 3$ independent experiments.

Fig. 5: Cryo-EM structure of the CCHFV L-suramin complex. a–b Cryo-EM density map (**a**) and atomic model (**b**) of the CCHFV L protein in complex with suramin. Two distinct suramin-binding sites are identified: site 1 (Suramin$^{1\#}$, green) located in the pocket

formed by the Core lobe and vRBL domains; and site 2 (Suramin$^{2\#}$, salmon) situated on the exterior surface of the Linker–Fingers domains. **c** Close-up of the cryo-EM density and atomic model (sticks) for Suramin$^{1\#}$ (top) and Suramin$^{2\#}$ (bottom) confirming the fit of the suramin molecules. Suramin$^{1\#}$ contains two suramin molecules (Suramin^{1A}, green; Suramin^{1B}, cyan); Suramin$^{2\#}$ contains three suramin molecules (Suramin^{2A}, magenta; Suramin^{2B}, salmon; Suramin^{2C}, red). **d** Detailed interactions at the first suramin-binding site (Suramin$^{1\#}$). The dimeric inhibitor forms an extensive network of interactions with residues in the vRBL and Core lobe, mimicking the interactions used to recognize the 5' vRNA. The protein is shown as a transparent cartoon. Suramin is shown as sticks and colored as in **c**. Hydrogen bonds or salt bridges are indicated by short dashed lines; cation–π interactions by long dashed lines. **e** Detailed interactions at the second suramin-binding site Suramin$^{2\#}$, involving residues from the Fingers and Linker domains. In (**d**) and (**e**), interacting side chains and suramin molecules are shown as sticks colored as in **c**. Hydrogen bonds or salt bridges are indicated by short dashed lines; cation–π interactions by long dashed lines.

Fig. 6: Structural basis of the CCHFV L–suramin interaction. a Close-up view of the Suramin$^{1\#}$ binding pocket (left). Superposition with the 5' vRNA-bound structure (right) reveals that Suramin$^{1\#}$ occupies the same pocket as the 5' vRNA hook, indicating a competitive binding mechanism. The RNA complex is colored as in **Fig. 3a**; the suramin-bound protein is shown as a transparent grey cartoon, with suramin colored as in **Fig. 5c**. **b** Competition BLI assays. Top, 5' vRNA binds to CCHFV L protein with high affinity (K_D < 1 pM). Bottom, pre-incubation with suramin abolishes 5' vRNA binding, confirming the steric blockade mechanism. **c** Detailed view of the Suramin$^{2\#}$ binding site. Comparison with the 5' vRNA-bound (middle) and apo states (right) suggests that Suramin$^{2\#}$ interacts with the linker and fingers domains. **d** Electrostatic surface representation of the Suramin$^{2\#}$ binding site, showing a positively charged surface that complements the assembly of trimeric suramin molecules rich in negatively charged sulfonate groups. Left, suramin molecules are shown as sticks against an opaque electrostatic surface; right, interacting residues are shown as sticks within a transparent electrostatic surface. **e** Structural alignment showing that Suramin$^{2\#}$ binding induces movement of the loop formed by residues 1652–1657 and stabilises residues 1671–1673 in the fingers domain.

Fig. 7: Binding affinity and inhibitory activity of suramin analogues against the CCHFV L protein. a Chemical structures of the suramin analogues NF023, NF157, NF449 and NF546. **b**–**e** SPR kinetic analysis of analogues binding to the CCHFV L protein. The calculated dissociation constants (K_D) are: 18.0 µM for NF023 (**b**); 25.2 µM for NF157 (**c**); 7.7 µM for NF449 (**d**); and 17.5 µM for NF546 (**e**). **f**–**l** *In vitro* polymerase activity assays showing concentration-dependent inhibition by each analogue. Data are representative of $n = 3$ independent experiments.

Fig. 8: Proposed model for CCHFV L protein function and inhibition. a In the resting state, the 5' vRNA hook binding pocket and the template/NTP entry tunnels are accessible; however, many structural elements remain flexible owing to the absence of stabilisation by the vRNA promoter. **b** In the working state, the 5' vRNA hook binds to its specific pocket, positioning the template in the active site and enabling the translocation of the RNA template and extrusion of the product RNA. **c** Inhibition by suramin occurs via a potent dual mechanism: 1) steric blockade, where Suramin$^{1\#}$ occupies the 5' vRNA hook binding pocket, preventing the initiation of viral replication; and 2) allosteric locking, in which Suramin$^{2\#}$ binds to the exterior surface of the linker–fingers domains, restricting the domain movements essential for the polymerase catalytic cycle.

Supplementary Fig. 1: Purification and functional characterization of the CCHFV L protein. a Size-exclusion chromatography (SEC) profile of the recombinant CCHFV L protein. The dashed box indicates the fraction collected for structural and functional studies. **b** SDS–PAGE analysis of the purified L protein, showing a predominant band corresponding to the expected molecular weight (~450 kDa). **c** Sequences of the RNA oligonucleotides used in this study. Black vertical lines indicate intramolecular hairpin formation within the 15-nt 5' vRNA and intermolecular complementary pairing with the 26-nt 3' vRNA template. **d** *In vitro* polymerase activity assay comparing metal ion cofactors. Product RNA synthesis is observed in the presence of 5 mM manganese (Mn^{2+}) but is negligible with magnesium (Mg^{2+}) under the same condition after incubation up to 2 hours. Data are representative of three independent experiments.

Supplementary Fig. 2: Cryo-EM data processing and reconstruction of apo CCHFV L protein. a Representative cryo-EM micrograph of the apo CCHFV L protein. Scale bar, 50 nm. **b** Data processing workflow. A total of 7,939 movies yielded 3,444,016 particles, which were subjected to 2D classification, *ab initio* reconstruction, and heterogeneous refinement to generate a final map from 48,496 particles. **c** Representative 2D class averages showing distinct orientations of the L protein. **d** Local resolution map of the final reconstruction shown in two views; the resolution color key is shown below. **e** Angular distribution plot of the particles included in the final reconstruction. **f** Gold-standard Fourier Shell Correlation (FSC) curve indicating a final global resolution of 2.59 Å at the 0.143 criterion.

Supplementary Fig. 3: Structural conservation of L proteins across the *Bunyavirales* order. Structural comparison of the CCHFV L protein (this work) with representative polymerases from the *Bunyavirales* order: SFTSV (*Phlebovirus;* PDB 8AS7), LACV (*Orthobunyavirus*; PDB 5AMR), HTNV (*Orthohantavirus*; PDB 8C4T), LASV (*Mammarenavirus*; PDB 7OJN) and MACV (*Mammarenavirus*; PDB 7EL9). The top row shows the full structures; subsequent rows display individual domains (linker–fingers, palm, core, thumb–thumb ring–lid, and vRBL) in identical orientations. The comparison highlighting the

high degree of structural conservation in the core machinery despite sequence divergence.

Supplementary Fig. 4: Cryo-EM data processing and reconstruction of the CCHFV L-vRNA complex. a Representative cryo-EM micrograph of the CCHFV L-vRNA complex. Scale bar, 50 nm. **b** Data processing workflow. Particles were picked from 4,848 movies using blob and template-based strategies, followed by multiple rounds of 2D classification, heterogeneous refinement and 3D classification. Non-uniform refinement of 66,103 particles yields a final map at 2.75 Å resolution. **c** Representative 2D class averages. **d** Local resolution map of the final reconstruction; the resolution color key is shown below. **e** Angular distribution of the particles used for the final reconstruction. **f** Gold-standard FSC curves indicating a final global resolution of 2.75 Å based on the FSC = 0.143 criterion.

Supplementary Fig. 5: Structural analysis of the CCHFV L–5' vRNA complex. a Cryo-EM density map of the L-5' vRNA complex. **b** Superposition of the atomic models of the apo (grey) and 5' vRNA-bound (colored by domain) states. Regions exhibiting significant structural differences—the vRBL (1), fingers (2) and arch (3) domains—are highlighted with dashed boxes in (**a**) and (**b**). **c** Structural superposition of the vRBL (magenta) and fingers (orange) domains from the RNA-bound state with the apo state (grey), highlighting the stabilization of flexible regions upon RNA binding. d Detailed comparison of the 5' vRNA binding pocket. Up: overall structural alignment of the 5' vRNA-bound (colored, opaque) and apo (grey, transparent) states. Bottom: close-up view of the key residues involved in vRNA binding. Side chains of interacting residues are shown as sticks and labeled; the RNA is shown as lime lines. **e** Electrostatic potential surface of the CCHFV L protein. The RNA-binding site is outlined with a solid black box and shown in the zoomed-in view . The 5' vRNA is depicted as a green cartoon. The electrostatic potential scale bar is shown below. **f** Structural comparison of the 5' vRNA binding pocket in CCHFV (this work) with HTNV (PDB 8C4T), LASV (PDB 7OJN), and LACV (PDB 5AMQ). The comparison demonstrates the conservation of the 5' vRNA binding mechanism across the *Bunyavirales* order. All structures are colored according to the CCHFV domain definitions, except for the unique pendant domain in LASV (colored forest green).

Supplementary Fig. 6: Affinity of nucleotide analogues for the CCHFV L protein. **a**–**b** Chemical structures of the antiviral nucleotide analogues tested: favipiravir (**a**), ribavirin (**b**), 2'-FdC (**c**) and obeldesivir (**d**). **e**–**h** Surface plasmon resonance (SPR) sensorgrams (left) and steady-state affinity fits (right) demonstrating that these compounds exhibit no significant binding to the CCHFV L protein at concentrations up to 20 µM, in contrast to the high affinity observed for suramin. Data are representative of n = 3 independent experiments.

Supplementary Fig. 7: Cryo-EM data processing and reconstruction of the CCHFV L-suramin complex. **a** Representative cryo-EM micrograph of the CCHFV L-suramin complex. Scale bar, 50 nm. **b** Workflow of cryo-EM data processing. Particles were picked from 5,547 movies using blob and template-based strategies. Following 2D classification, heterogeneous refinement and 3D classification, a final set of 37,822 particles was subjected to non-uniform refinement, resulting in a density map at 2.50 Å resolution. **c** Representative 2D class averages of the L-suramin complex particles. **d** Local resolution map of the final reconstruction; the resolution color key is shown below. **e** Angular distribution of the particles used in the final reconstruction. **f** Gold-standard FSC curves indicating a final global resolution of 2.50 Å at the FSC = 0.143 threshold.

Supplementary Fig. 8: Schematic representation of interactions in the CCHFV L–suramin complex. **a** Chemical structure of the symmetrical suramin molecule. The naphthalene (A, B) and benzene (C, D) rings are labeled; primes (') denote the corresponding rings on the symmetrical side. **b** Intermolecular interactions between suramin molecules within the binding assemblies. Left: Site 1 (Suramin$^{1\#}$), showing interactions within the suramin dimer. Right: Site 2 (Suramin$^{2\#}$), showing interactions within the suramin trimer assembly. **c**–**d** Schematic representations of the interactions between the L protein and two suramin assemblies. Only amino acid residues involved in direct interactions are shown. Hydrogen bonds and salt bridges are indicated by black dashed lines. π–π interactions (in **b**) and cation–π interactions (in **c** and **d**) are depicted as

grey double lines. The coloring of suramin molecules and protein residues is consistent with the main text figures.

Supplementary Fig. 9: Conformational analysis of residues at the suramin–L protein interface. a Structural superposition of the suramin-bound state with the apo state (up) and the RNA-bound state (bottom) at Site 1 (Suramin$^{1\#}$). Residue K1379 undergoes a significant conformational shift, pulling the adjacent loop towards the inhibitor. Other residues involved in suramin binding exhibit minimal structural changes compared to the apo or RNA-bound states. However, the comparison in bottom confirms that suramin physically occupies the RNA-binding pocket, creating severe steric clashes. Residues R1252, Y1399, Q1517, S1549 and R1551 are shared recognition residues for both suramin and the 5' vRNA. **b** Structural superposition of the suramin-bound (colored), apo (black), and 5' vRNA-bound (grey) states. Relative to the apo state, RNA binding induces a slight expansion of the architecture, whereas suramin binding causes contraction. Labels 1, 2 and 3 indicate the relative positions of the same site in the suramin-bound, apo and RNA-bound states, respectively. **c** Superposition of the Suramin-bound and apo states at Site 2 (Suramin$^{2\#}$). Suramin binding stabilizes residues K1672 and A1673, and induces conformational changes in K1655, K1656 and R1671. The engagement of K1655 and K1656 specifically triggers a shift of the hosting loop towards the drug, while other residues remain largely unchanged.

Supplementary Fig. 10: Comparison of suramin binding and inhibition mechanisms across viral RNA polymerases. a Structure of the CCHFV L protein bound to suramin (this work), showing the dual binding sites: Suramin$^{1\#}$ within the 5' vRNA binding pocket and Suramin$^{2\#}$ on the exterior surface of the linker–fingers domains. **b** Suramin binding to the Ebola virus (EBOV) L–VP35 polymerase complex (PDB 7YET). Suramin binds within the NTP entry channel, physically blocking the entry of substrates into the active site. **c** Suramin binding to the SARS-CoV-2 RdRp (PDB 7D4F). Two suramin molecules bind within the catalytic chamber, blocking the binding of both the RNA template and primer strands. **d** Suramin binding to the Norovirus RdRp (PDB 3UR0). Suramin binds in the cleft between the fingers and thumb domains, preventing the

positioning of the RNA template for initiation. The comparison highlights that the binding sites and inhibition mechanism identified in the CCHFV L protein are distinct from the active-site or channel-blocking mechanisms reported for other viral polymerases. Proteins are shown as transparent cartoons colored by domain (corresponding to the CCHFV structure); suramin is shown as green sticks.

Supplementary Fig. 11: Structural model of the CCHFV L protein replication cycle. Proposed conformational states of the CCHFV L protein during the viral replication cycle, modeled on homologous structures from the *Bunyavirales* order. The cycle transitions from the inactive or resting state (based on PDB 5AMQ) to the pre-initiation state (based on PDB 7ORJ), in which the 5' vRNA hook is bound. Subsequent stages include the early elongation state (based on PDB 7ORM), showing product RNA formation, and the late elongation state (based on PDB 8AS7), where the product exits the polymerase. The paths of the 5' vRNA hook (green), 3' vRNA template (cyan) and product RNA (yellow) are indicated. Incoming NTPs are depicted as red spheres, and the location of the active site is marked.

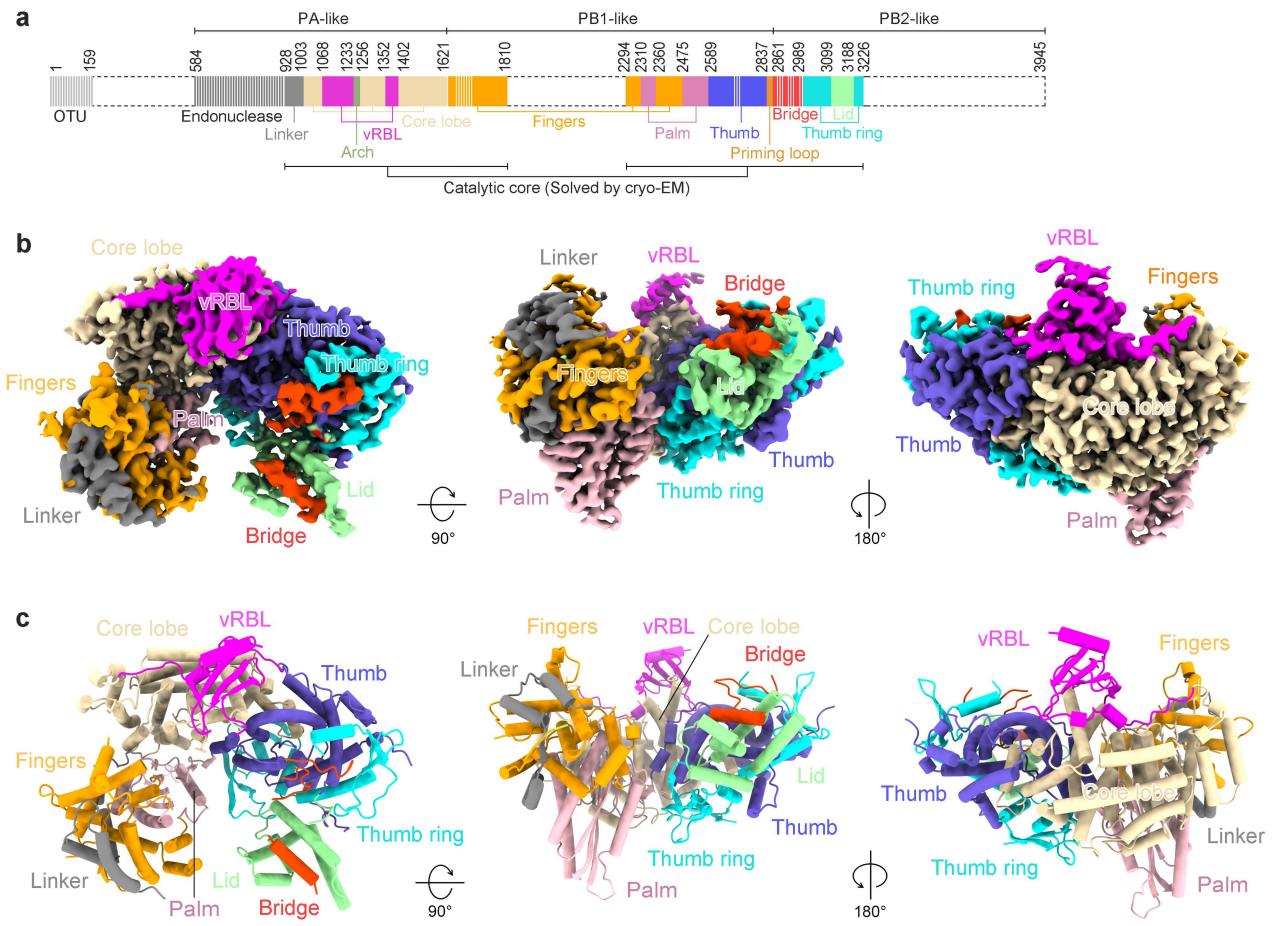

Fig. 1: Cryo-EM structure of the Crimean-Congo hemorrhagic fever virus (CCHFV) L protein. a Domain architecture of the CCHFV L protein. Domain assignments are based on structural conservation among viral RNA polymerases of the order *Bunyavirales*. Domains are colored as follows: Linker (grey), Core lobe (wheat), vRBL (magenta), Arch (smudge), Fingers (orange), Palm (pink), Thumb (slate), Bridge (red), Thumb ring (cyan) and Lid (green). Residue boundaries are indicated above. Solid bars indicate regions resolved by cryo-EM; grey hatched bars represent known functional domains (OTU and endonuclease) that were not resolved. Structurally and functionally uncharacterized regions are shown in white. Regions corresponding to PA, PB1 and PB2 are indicated. **b** Cryo-EM density maps of the apo CCHFV L protein shown in three orthogonal views and colored according to the domain scheme in (**a**). Key structural features are labeled. **c** Cartoon representation of the CCHFV L protein in the same orientations as (**b**), with domains colored accordingly.

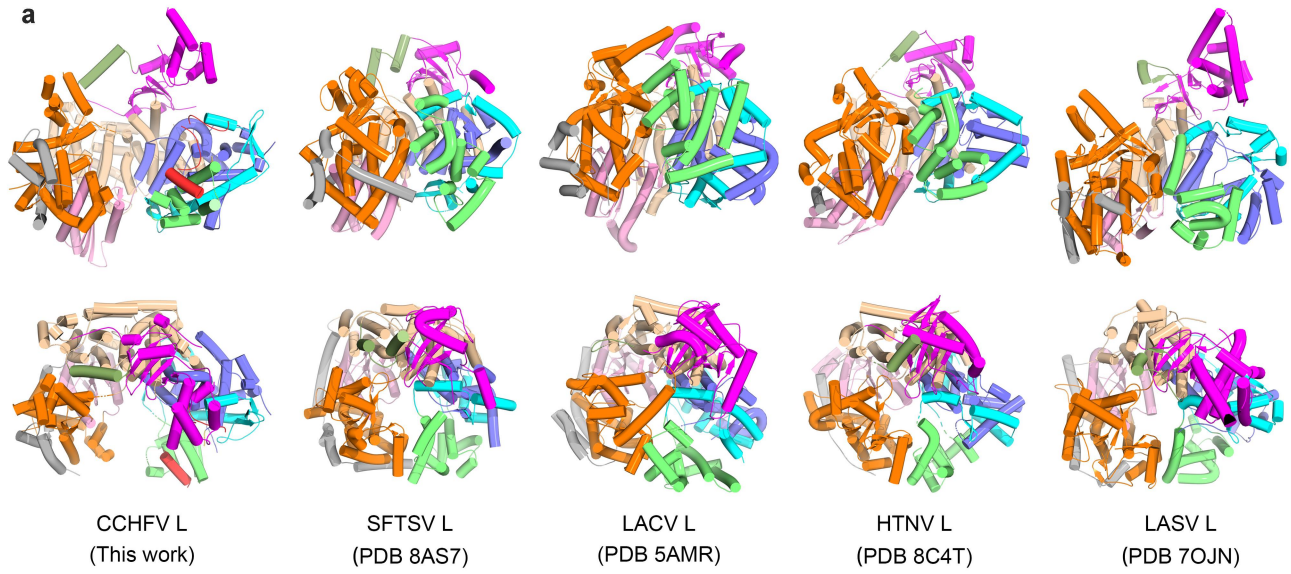
a
CCHFV L
(This work)
SFTSV L
(PDB 8AS7)
LACV L
(PDB 5AMR)
HTNV L
(PDB 8C4T)
LASV L
(PDB 7OJN)

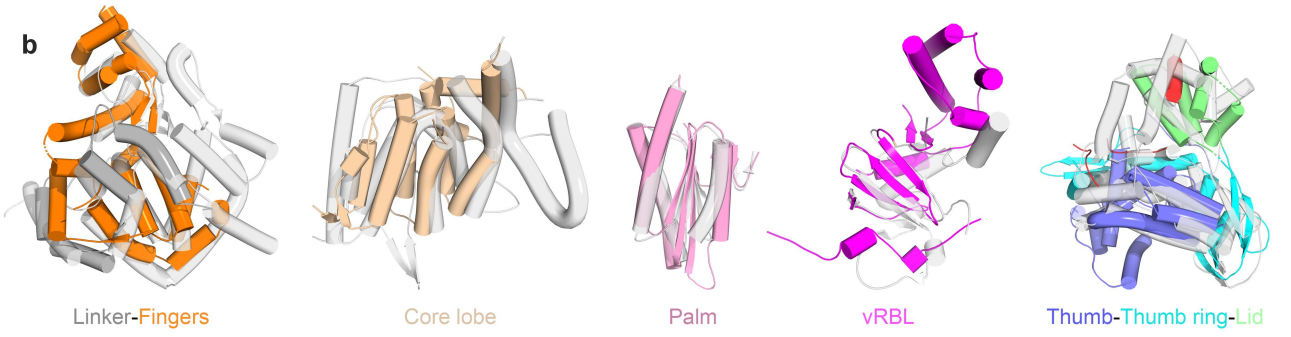
b
Linker-Fingers
Core lobe
Palm
vRBL
Thumb-Thumb ring-Lid

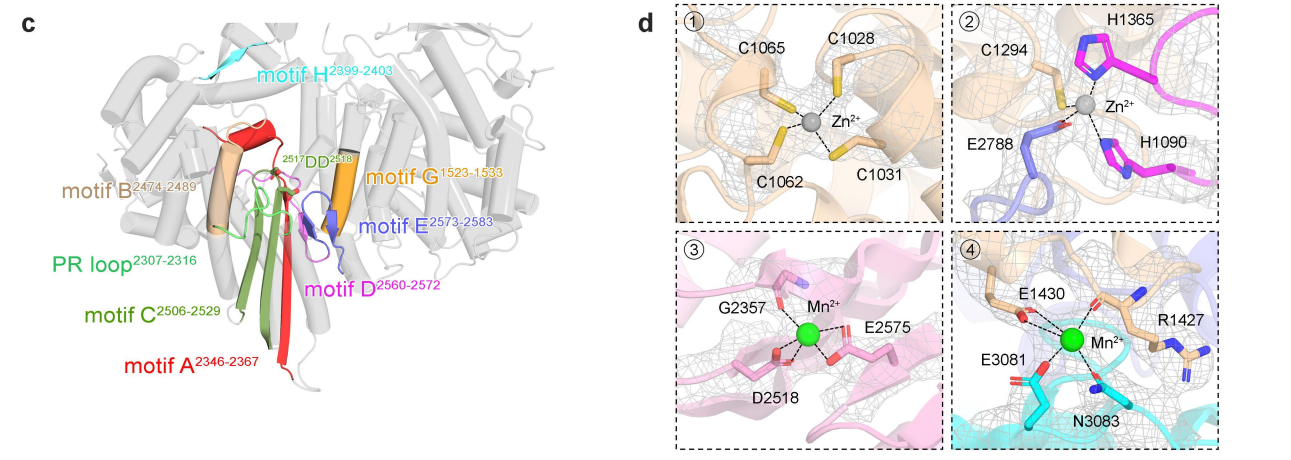
c
motif H2399-2403
2517DD2518
motif G1523-1533
motif B2474-2489
motif E2573-2583
PR loop2307-2316
motif D2560-2572
motif C2506-2529
motif A2346-2367
d
1
C1065
C1028
Zn2+
C1062
C1031
2
H1365
C1294
Zn2+
E2788
H1090
3
G2357
Mn2+
E2575
D2518
4
E1430
R1427
Mn2+
E3081
N3083

Fig. 2: Structure and conservation of the CCHFV L protein. a Structural comparison of the CCHFV L protein (this work) with other polymerases of the order *Bunyavirales*: SFTSV (PDB 8AS7), LACV (PDB 5AMR), HTNV (PDB 8C4T), and LASV (PDB 7OJN). The overall fold is highly conserved across the *Nairovirus*, *Phlebovirus*, *Orthobunyavirus*, *Orthohantavirus*, and *Mammarenavirus* genera. **b** Detailed structural superposition of individual segments (Linker–Fingers, Core lobe, Palm, vRBL, Thumb-Thumb ring-Lid), highlighting the similarity of secondary structural elements. **c** Conservation of key RdRp catalytic motifs and loops. The arrangement of conserved viral RdRp motifs A–H and the Prime-and-Realign (PR) loop is shown; each motif is colored differently with its amino acid range labelled. Motif F and the priming loop were not resolved. Key residues D2517 and D2518 are shown as sticks. **d** Four metal ions identified in the cryo-EM density map, including two zinc (Zn^{2+}) and two (Mn^{2+}) ions. Panels 1 and 2 show two structural Zn^{2+} ions coordinated by C1028/C1031/C1062/C1065 and H1090/C1294/H1365/E2788, respectively. Panels 3 and 4 show two Mn^{2+} ions coordinated by G2357/D2518/E2575 and R1427/E1430/E3081/N3083.

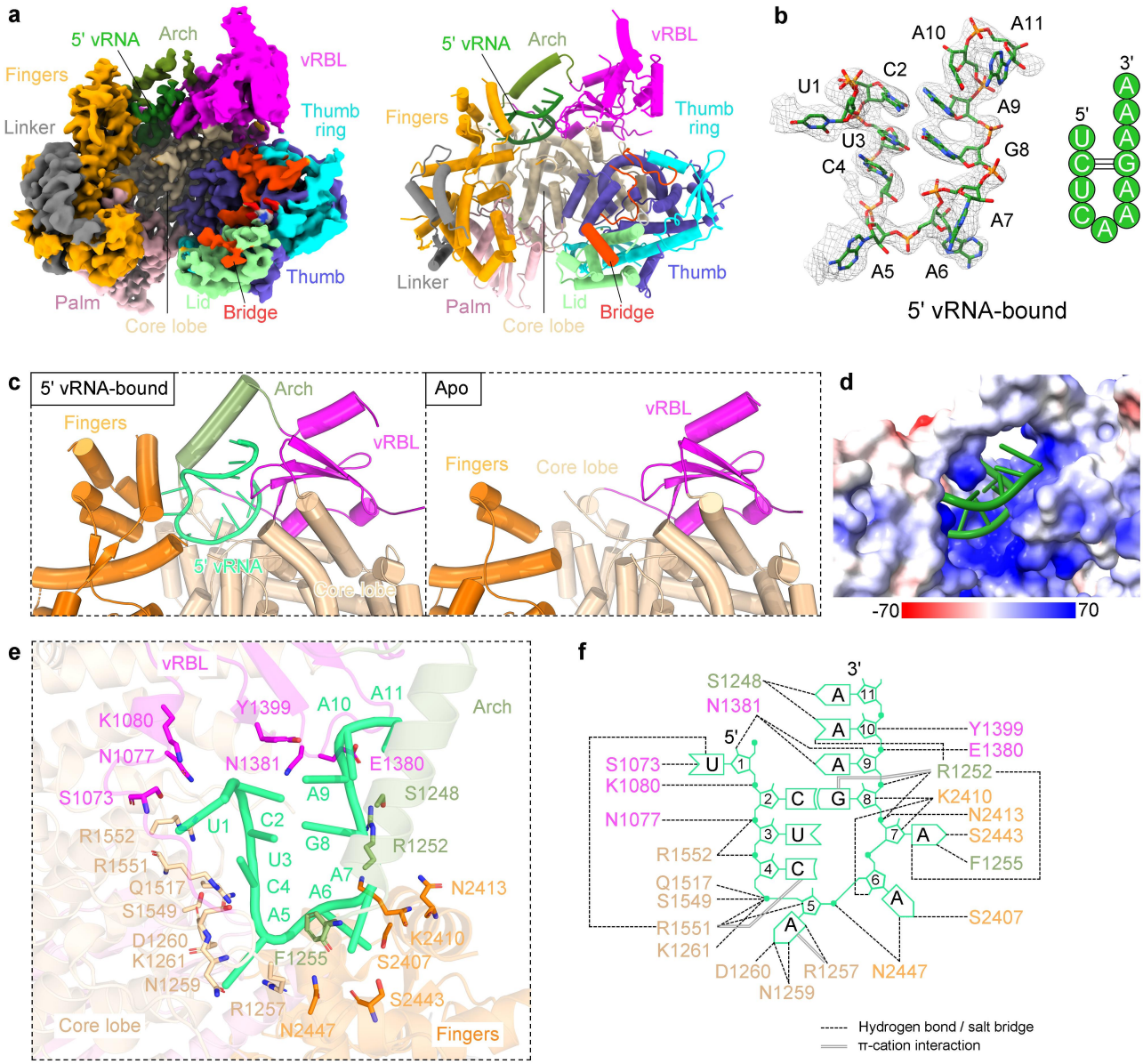

Fig. 3: Recognition of the 5' vRNA hook by the CCHFV L protein. a Overall view of the CCHFV L protein (colored as in **Fig. 1**) in complex with the 5' vRNA (green). Left, cryo-EM density map; right, atomic model in cartoon representation. The RNA binds in a pocket formed by the vRBL, Arch, Fingers, and Core lobe domains. **b** Cryo-EM density map (mesh) and atomic model (sticks) of the 5' vRNA, which adopts a characteristic stem-loop "hook" structure formed by base pairing between nucleotides C2-G8. **c** Close-up view of the 5' vRNA binding pocket. Structural comparison of the 5' vRNA-bound state (left) and the apo state (right) shows that RNA binding induces local conformational stabilisation in the arch, vRBL and fingers domains. **d** Electrostatic potential surface of the RNA-binding cleft showing that the 5' vRNA hook binds into a highly basic cavity. Scale bar is shown. **e** Detailed interaction network recognizing the 5' vRNA. Interacting residues are shown as sticks and labelled; RNA is shown as a cartoon and the protein backbone as a transparent cartoon. **f** Schematic diagram summarizing the intermolecular contacts between L protein residues and the 5' vRNA nucleotides. Hydrogen bonds and salt bridges are indicated by dashed lines; cation–π interactions by double solid lines.

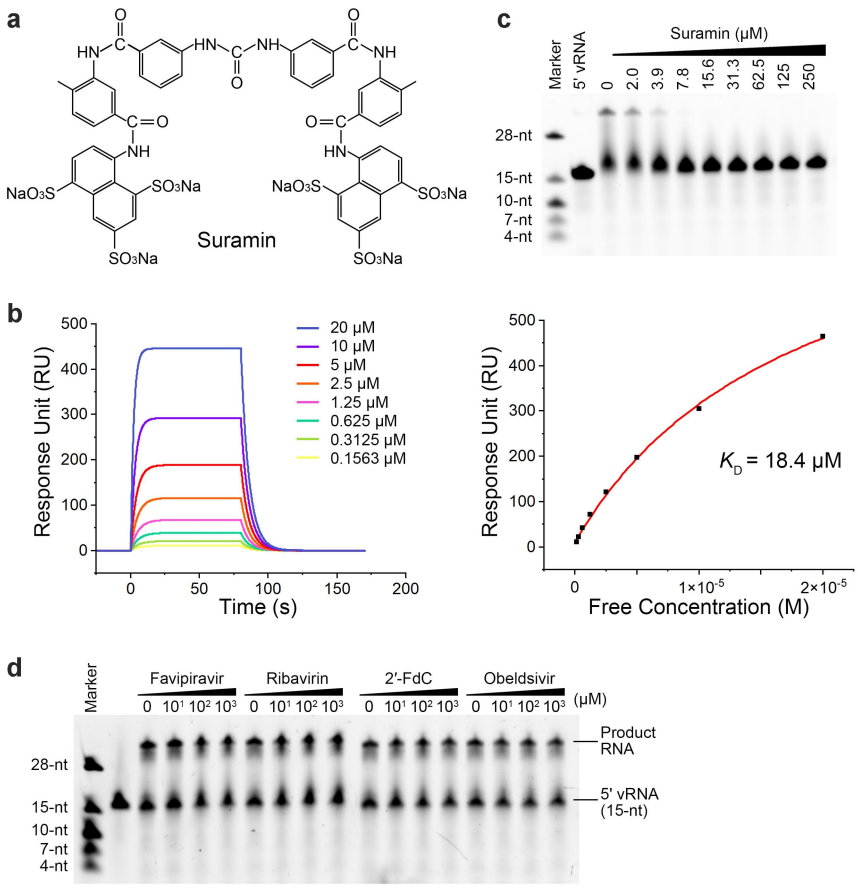

Fig. 4: Suramin is a potent inhibitor of the CCHFV L protein. a Chemical structure of suramin. **b** Surface plasmon resonance (SPR) analysis of suramin binding to the CCHFV L protein. Left, sensorgrams showing binding at increasing concentrations (0.1563–20 μM). Right, steady-state affinity fitting yielding a dissociation constant (K_D) of 18.4 μM. **c** *In vitro* polymerase activity assay showing dose-dependent inhibition of RNA synthesis by suramin. The production of RNA products longer than 28 nt decreases with increasing suramin concentration. **d** *In vitro* polymerase activity assay of nucleotide analogues against the CCHFV L protein. Activity is not inhibited by favipiravir, ribavirin, 2'-FdC or obeldesivir at concentrations up to 1 mM. Data are representative of n = 3 independent experiments.

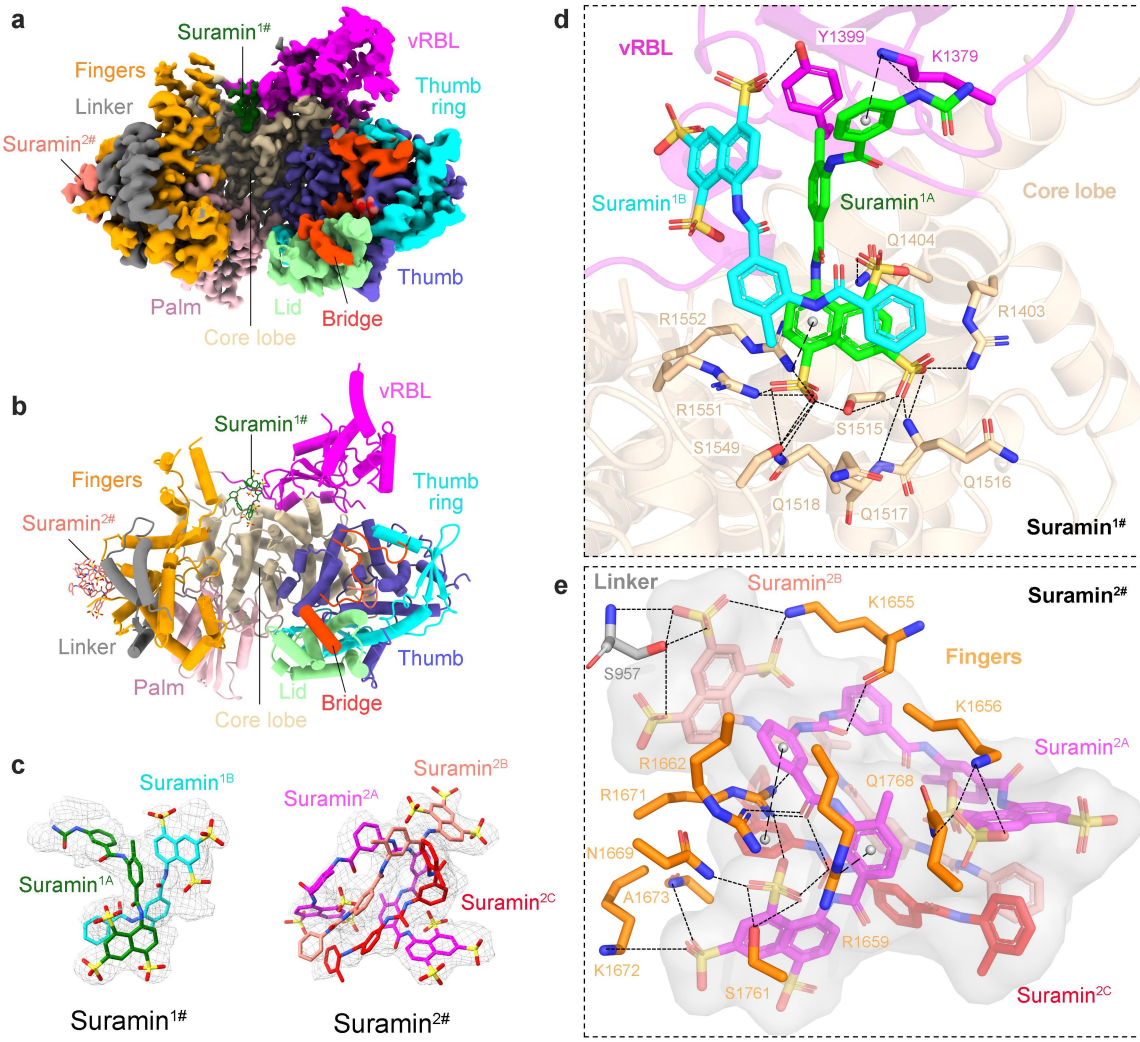

Fig. 5: Cryo-EM structure of the CCHFV L-suramin complex. a–**b** Cryo-EM density map (**a**) and atomic model (**b**) of the CCHFV L protein in complex with suramin. Two distinct suramin-binding sites are identified: site 1 (Suramin$^{1\#}$, green) located in the pocket formed by the Core lobe and vRBL domains; and site 2 (Suramin$^{2\#}$, salmon) situated on the exterior surface of the Linker–Fingers domains. **c** Close-up of the cryo-EM density and atomic model (sticks) for Suramin$^{1\#}$ (top) and Suramin$^{2\#}$ (bottom) confirming the fit of the suramin molecules. Suramin$^{1\#}$ contains two suramin molecules (Suramin^{1A}, green; Suramin^{1B}, cyan); Suramin$^{2\#}$ contains three suramin molecules (Suramin^{2A}, magenta; Suramin^{2B}, salmon; Suramin^{2C}, red). **d** Detailed interactions at the first suramin-binding site (Suramin$^{1\#}$). The dimeric inhibitor forms an extensive network of interactions with residues in the vRBL and Core lobe, mimicking the interactions used to recognize the 5' vRNA. The protein is shown as a transparent cartoon. Suramin is shown as sticks and colored as in **c**. Hydrogen bonds or salt bridges are indicated by short dashed lines; cation–π interactions by long dashed lines. **e** Detailed interactions at the second suramin-binding site Suramin$^{2\#}$, involving residues from the Fingers and Linker domains. In (**d**) and (**e**), interacting side chains and suramin molecules are shown as sticks colored as in **c**. Hydrogen bonds or salt bridges are indicated by short dashed lines; cation–π interactions by long dashed lines.

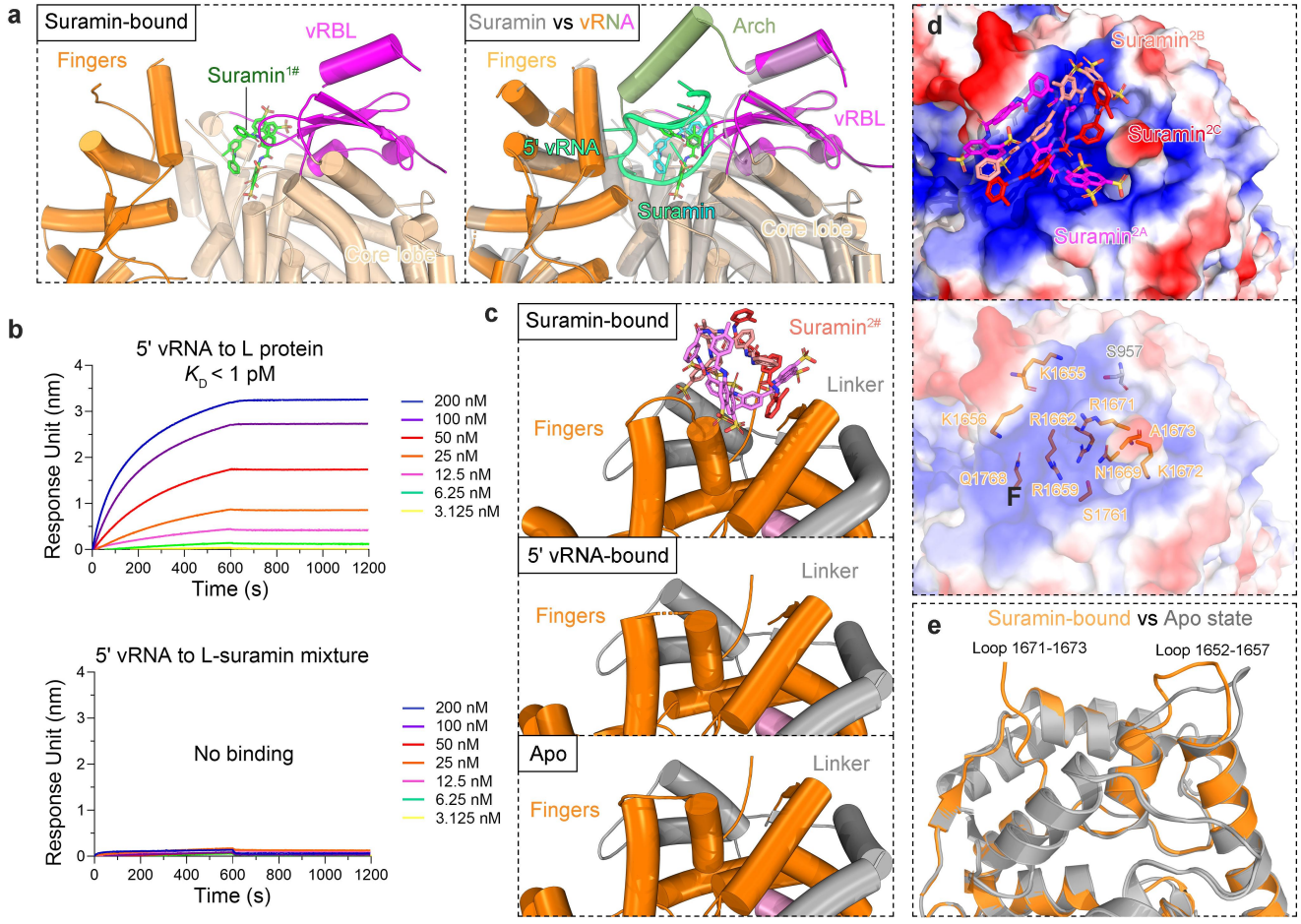

Fig. 6: Structural basis of the CCHFV L–suramin interaction. a Close-up view of the Suramin$^{1\#}$ binding pocket (left). Superposition with the 5' vRNA-bound structure (right) reveals that Suramin$^{1\#}$ occupies the same pocket as the 5' vRNA hook, indicating a competitive binding mechanism. The RNA complex is colored as in **Fig. 3a**; the suramin-bound protein is shown as a transparent grey cartoon, with suramin colored as in **Fig. 5c**. **b** Competition BLI assays. Top, 5' vRNA binds to CCHFV L protein with high affinity (K_D < 1 pM). Bottom, pre-incubation with suramin abolishes 5' vRNA binding, confirming the steric blockade mechanism. **c** Detailed view of the Suramin$^{2\#}$ binding site. Comparison with the 5' vRNA-bound (middle) and apo states (right) suggests that Suramin$^{2\#}$ interacts with the linker and fingers domains. **d** Electrostatic surface representation of the Suramin$^{2\#}$ binding site, showing a positively charged surface that complements the assembly of trimeric suramin molecules rich in negatively charged sulfonate groups. Left, suramin molecules are shown as sticks against an opaque electrostatic surface; right, interacting residues are shown as sticks within a transparent electrostatic surface. **e** Structural alignment showing that Suramin$^{2\#}$ binding induces movement of the loop formed by residues 1652–1657 and stabilises residues 1671–1673 in the fingers domain.

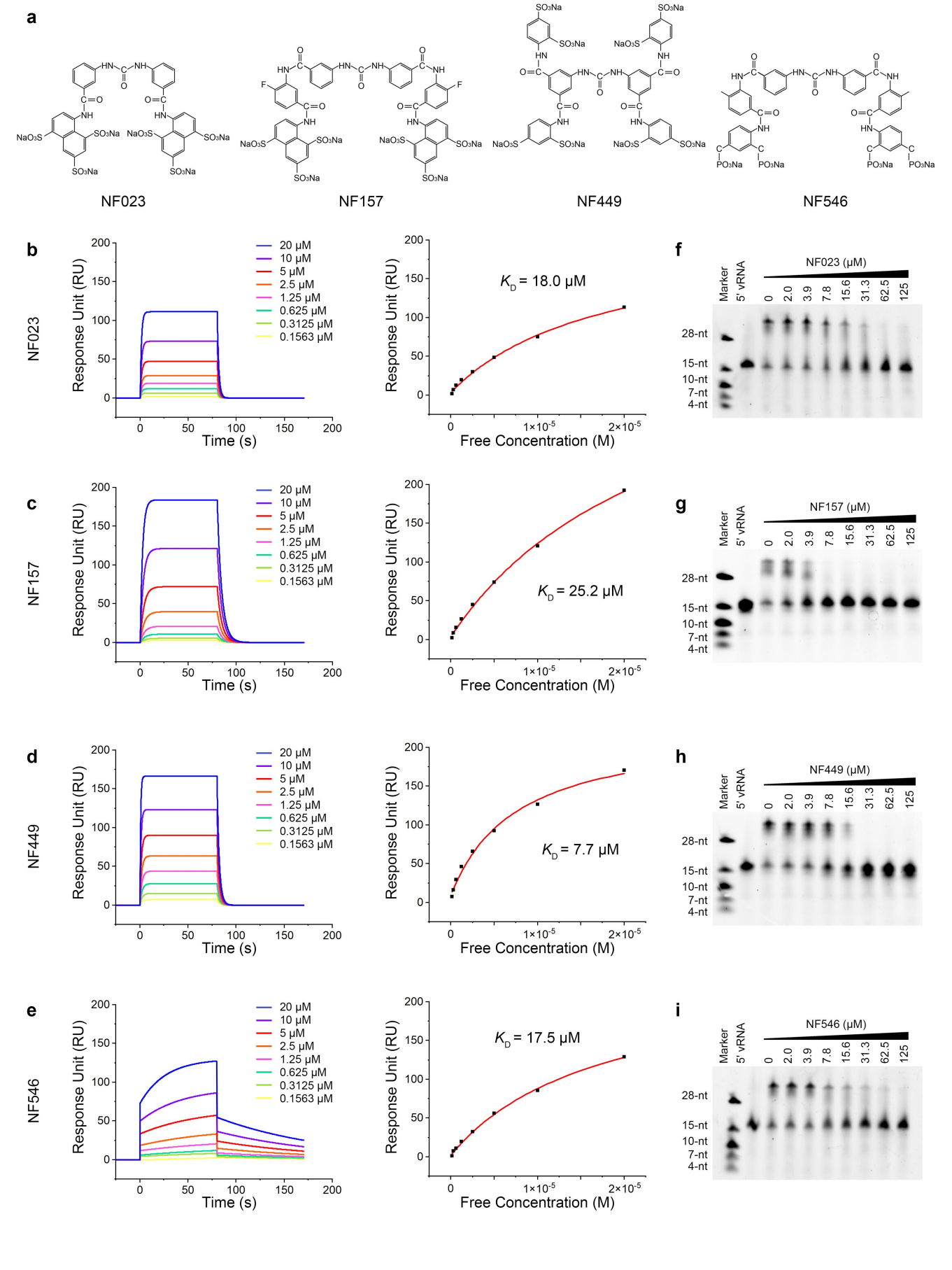
a
NF023
NF157
NF449
NF546
b
NF023
Response Unit (RU)
Time (s)
20 μM
10 μM
5 μM
2.5 μM
1.25 μM
0.625 μM
0.3125 μM
0.1563 μM
K_D = 18.0 μM
Free Concentration (M)
c
NF157
K_D = 25.2 μM
d
NF449
K_D = 7.7 μM
e
NF546
K_D = 17.5 μM
f
NF023 (μM)
g
NF157 (μM)
h
NF449 (μM)
i
NF546 (μM)
Marker
5' vRNA
0
2.0
3.9
7.8
15.6
31.3
62.5
125
28-nt
15-nt
10-nt
7-nt
4-nt

Fig. 7: Binding affinity and inhibitory activity of suramin analogues against the CCHFV L protein. a Chemical structures of the suramin analogues NF023, NF157, NF449 and NF546. **b**–**e** SPR kinetic analysis of analogues binding to the CCHFV L protein. The calculated dissociation constants (K_D) are: 18.0 μM for NF023 (**b**); 25.2 μM for NF157 (**c**); 7.7 μM for NF449 (**d**); and 17.5 μM for NF546 (**e**). **f**–**l** *In vitro* polymerase activity assays showing concentration-dependent inhibition by each analogue. Data are representative of $n = 3$ independent experiments.

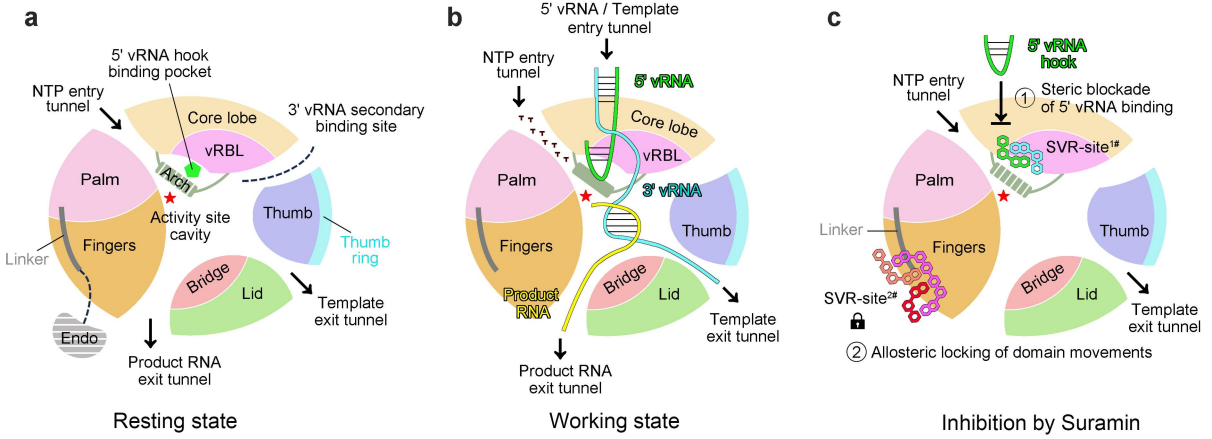

Fig. 8: Proposed model for CCHFV L protein function and inhibition. a In the resting state, the 5' vRNA hook binding pocket and the template/NTP entry tunnels are accessible; however, many structural elements remain flexible owing to the absence of stabilisation by the vRNA promoter. **b** In the working state, the 5' vRNA hook binds to its specific pocket, positioning the template in the active site and enabling the translocation of the RNA template and extrusion of the product RNA. **c** Inhibition by suramin occurs via a potent dual mechanism: 1) steric blockade, where Suramin$^{1\#}$ occupies the 5' vRNA hook binding pocket, preventing the initiation of viral replication; and 2) allosteric locking, in which Suramin$^{2\#}$ binds to the exterior surface of the linker–fingers domains, restricting the domain movements essential for the polymerase catalytic cycle.

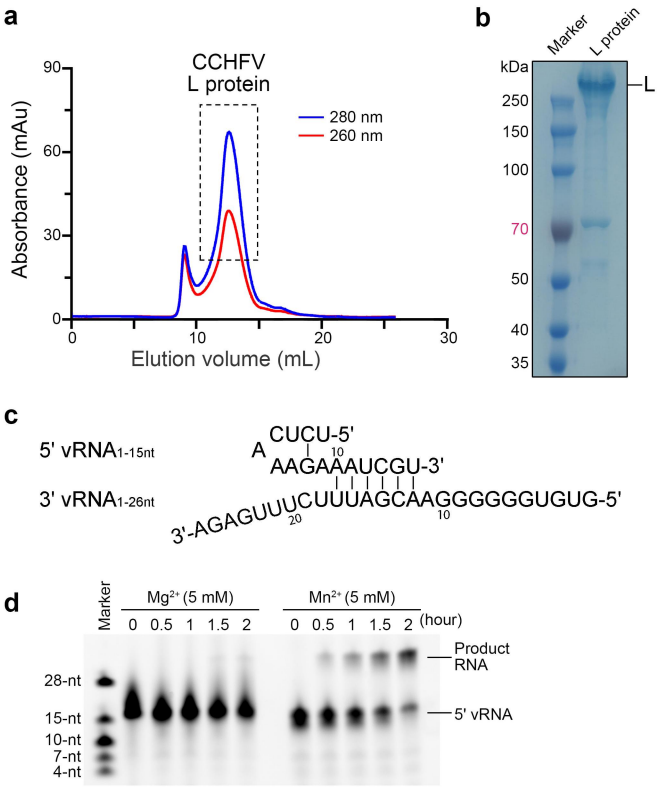

Supplementary Fig. 1: Purification and functional characterization of the CCHFV L protein. a Size-exclusion chromatography (SEC) profile of the recombinant CCHFV L protein. The dashed box indicates the fraction collected for structural and functional studies. **b** SDS–PAGE analysis of the purified L protein, showing a predominant band corresponding to the expected molecular weight (~450 kDa). **c** Sequences of the RNA oligonucleotides used in this study. Black vertical lines indicate intramolecular hairpin formation within the 15-nt 5' vRNA and intermolecular complementary pairing with the 26-nt 3' vRNA template. **d** *In vitro* polymerase activity assay comparing metal ion cofactors. Product RNA synthesis is observed in the presence of 5 mM manganese (Mn^{2+}) but is negligible with magnesium (Mg^{2+}) under the same condition after incubation up to 2 hours. Data are representative of three independent experiments.

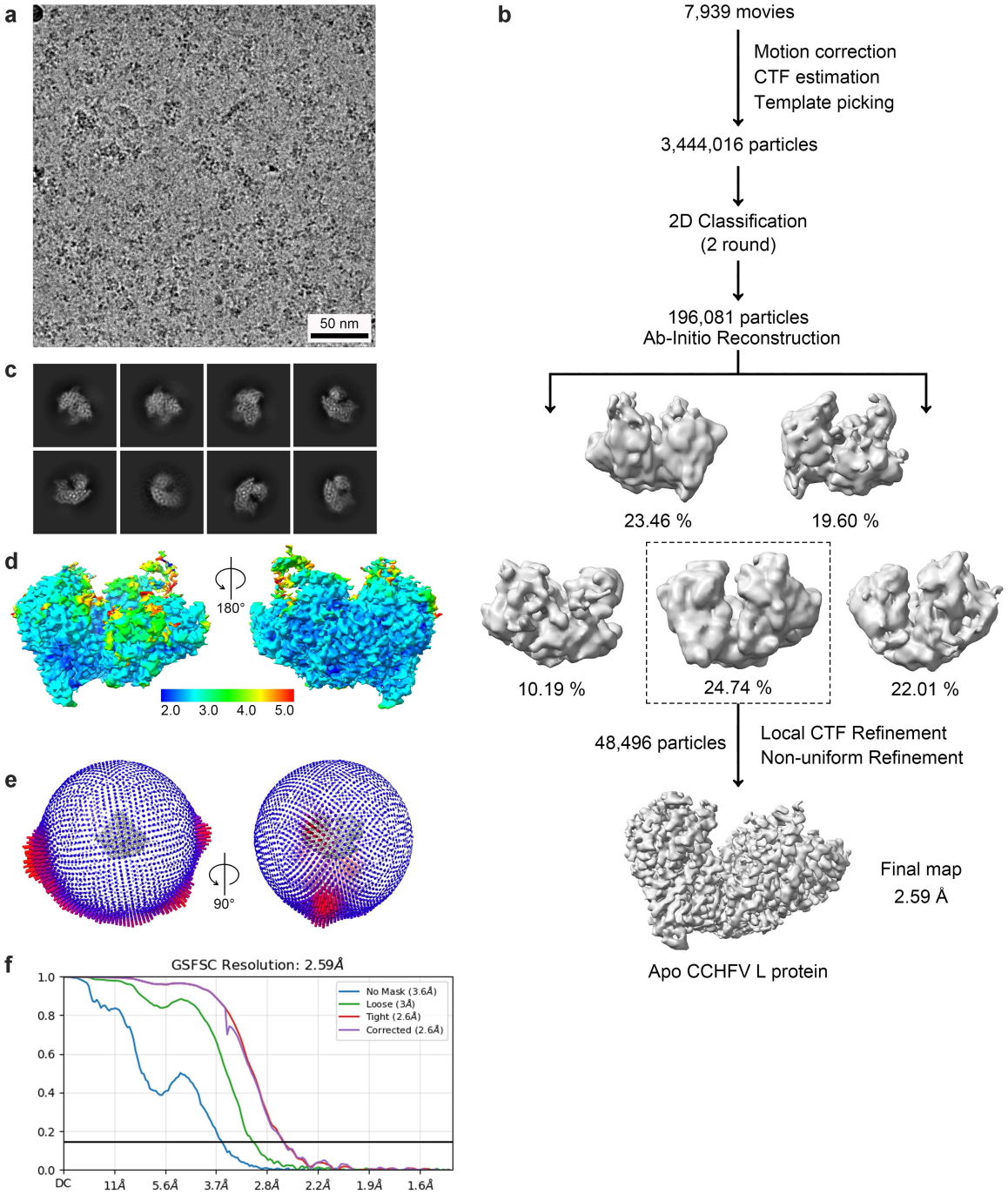

Supplementary Fig. 2: Cryo-EM data processing and reconstruction of apo CCHFV L protein. a Representative cryo-EM micrograph of the apo CCHFV L protein. Scale bar, 50 nm. **b** Data processing workflow. A total of 7,939 movies yielded 3,444,016 particles, which were subjected to 2D classification, *ab initio* reconstruction, and heterogeneous refinement to generate a final map from 48,496 particles. **c** Representative 2D class averages showing distinct orientations of the L protein. **d** Local resolution map of the final reconstruction shown in two views; the resolution color key is shown below. **e** Angular distribution plot of the particles included in the final reconstruction. **f** Gold-standard Fourier Shell Correlation (FSC) curve indicating a final global resolution of 2.59 Å at the 0.143 criterion.

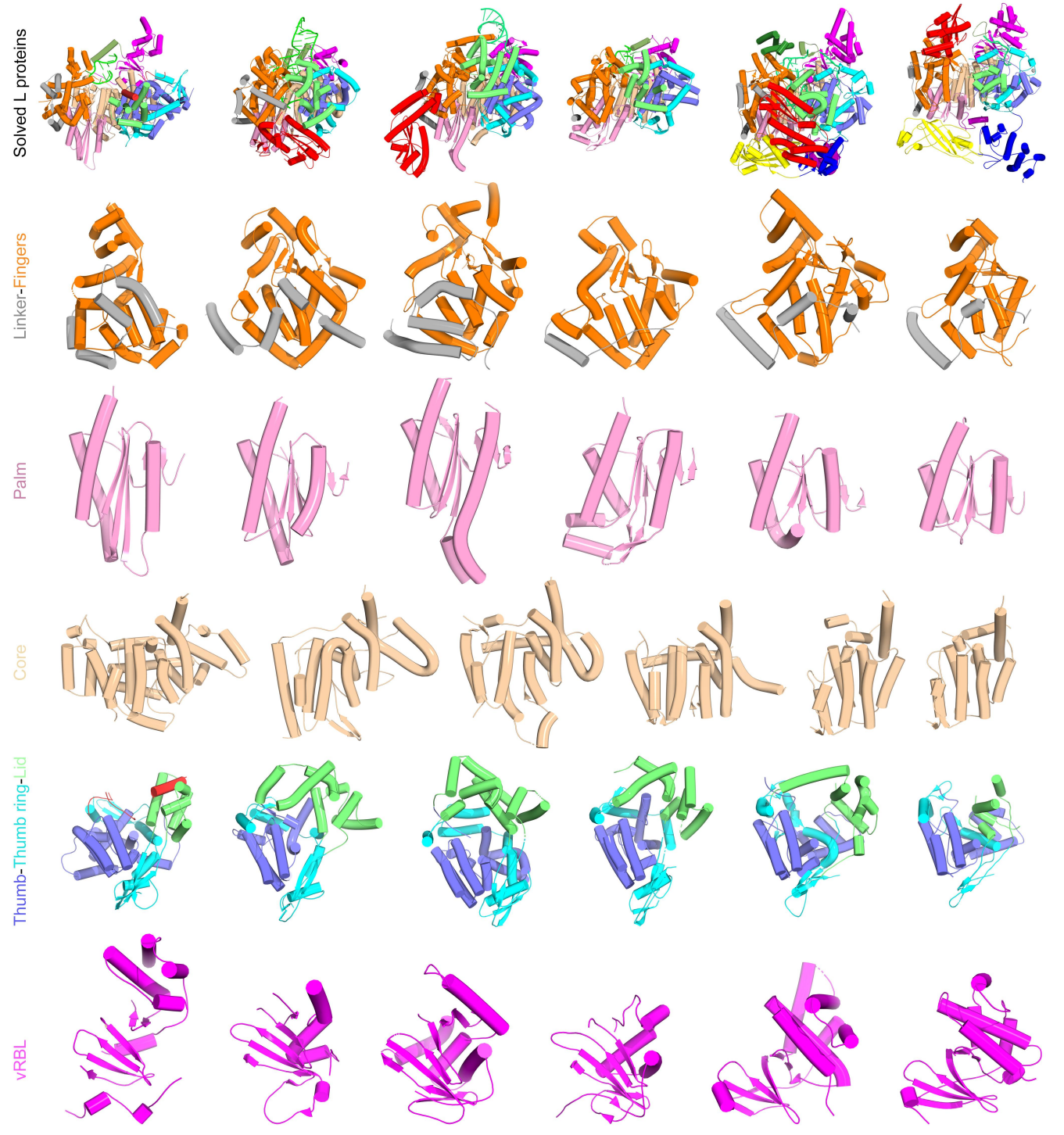
Solved L proteins
Linker-Fingers
Palm
Core
Thumb-Thumb ring-Lid
vRBL
CCHFV L
(This work)
Nairovirus
SFTSV L
(PDB 8AS7)
Phlebovirus
Phenuiviridae
LACV L
(PDB 5AMR)
Orthobunyavirus
Bunyaviridae
HNTV L
(PDB 8C4T)
Orthohantavirus
Hantaviridae
LASV L
(PDB 7OJN)
MACV L
(PDB 7EL9)
Mammarenavirus
Arenaviridae

Supplementary Fig. 3: Structural conservation of L proteins across the *Bunyavirales* order. Structural comparison of the CCHFV L protein (this work) with representative polymerases from the *Bunyavirales* order: SFTSV (*Phlebovirus;* PDB 8AS7), LACV (*Orthobunyavirus*; PDB 5AMR), HTNV (*Orthohantavirus*; PDB 8C4T), LASV (*Mammarenavirus*; PDB 7OJN) and MACV (*Mammarenavirus*; PDB 7EL9). The top row shows the full structures; subsequent rows display individual domains (linker–fingers, palm, core, thumb–thumb ring–lid, and vRBL) in identical orientations. The comparison highlighting the high degree of structural conservation in the core machinery despite sequence divergence.

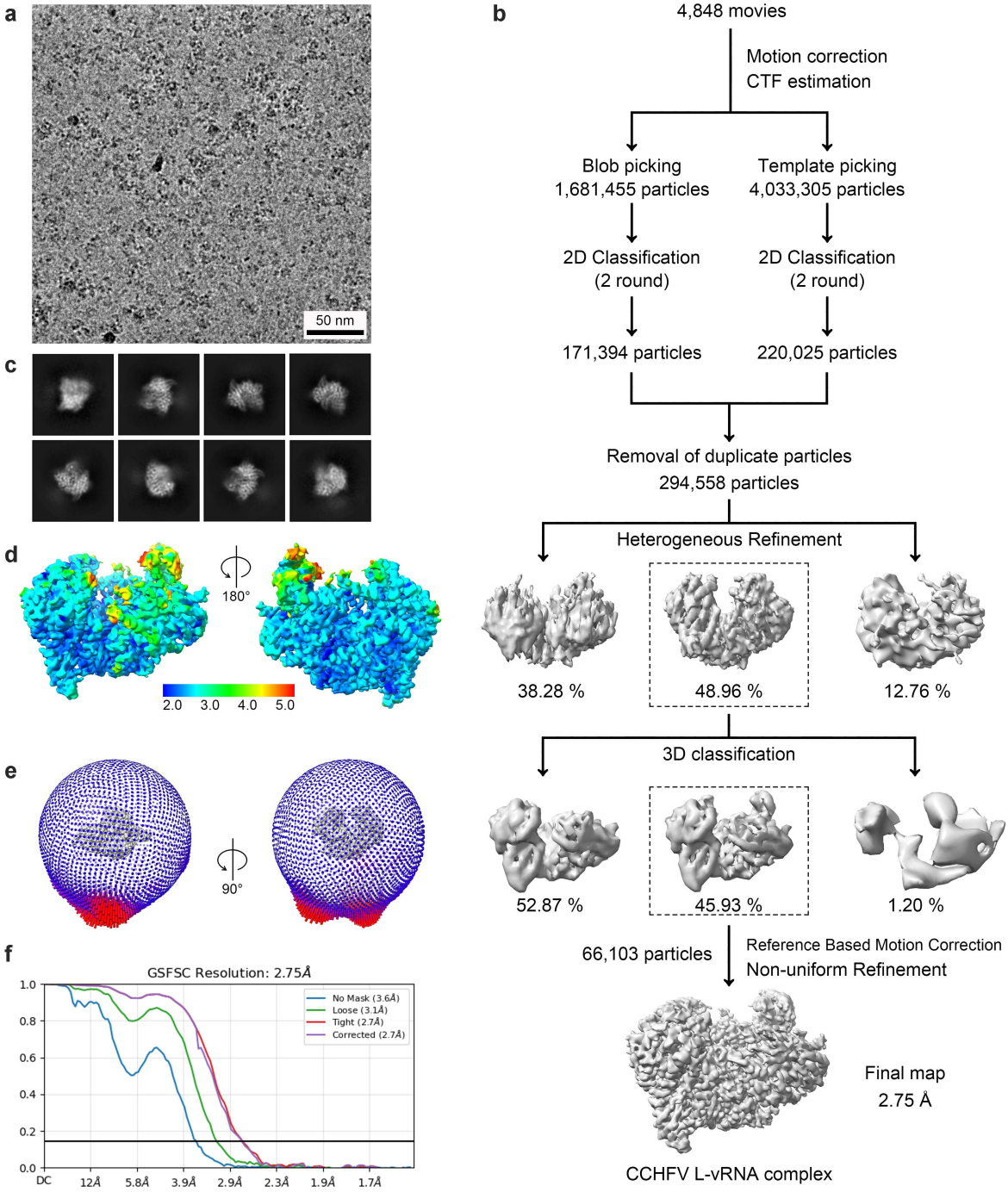

Supplementary Fig. 4: Cryo-EM data processing and reconstruction of the CCHFV L-vRNA complex. a Representative cryo-EM micrograph of the CCHFV L-vRNA complex. Scale bar, 50 nm. **b** Data processing workflow. Particles were picked from 4,848 movies using blob and template-based strategies, followed by multiple rounds of 2D classification, heterogeneous refinement and 3D classification. Non-uniform refinement of 66,103 particles yields a final map at 2.75 Å resolution. **c** Representative 2D class averages. **d** Local resolution map of the final reconstruction; the resolution color key is shown below. **e** Angular distribution of the particles used for the final reconstruction. **f** Gold-standard FSC curves indicating a final global resolution of 2.75 Å based on the FSC = 0.143 criterion.

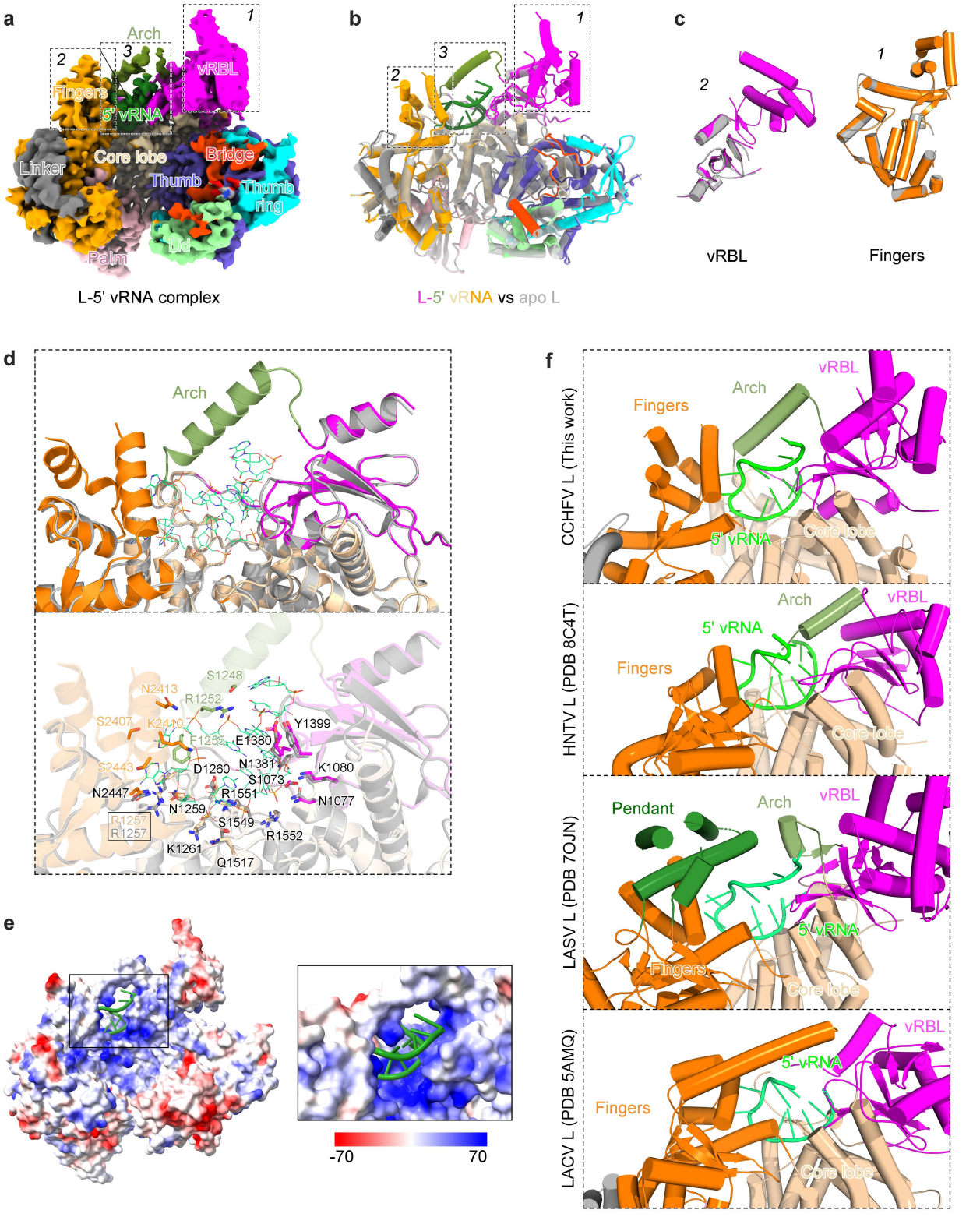
a
Arch
1
2
3
vRBL
Fingers
5' vRNA
Linker
Core lobe
Bridge
Thumb
Thumb ring
Lid
Palm
L-5' vRNA complex
b
1
3
2
L-5' vRNA vs apo L
c
2
1
vRBL
Fingers
d
Arch
S1248
N2413
R1252
S2407
K2410
Y1399
F1255
E1380
S2443
D1260
N1381
K1080
S1073
N2447
R1551
N1077
N1259
S1549
R1257
R1257
R1552
K1261
Q1517
e
-70
70
f
CCHFV L (This work)
vRBL
Arch
Fingers
5' vRNA
Core lobe
HNTV L (PDB 8C4T)
Arch
vRBL
5' vRNA
Fingers
Core lobe
LASV L (PDB 7OJN)
Pendant
Arch
vRBL
5' vRNA
Fingers
Core lobe
LACV L (PDB 5AMQ)
vRBL
5' vRNA
Fingers
Core lobe

Supplementary Fig. 5: Structural analysis of the CCHFV L–5' vRNA complex. a Cryo-EM density map of the L-5' vRNA complex. **b** Superposition of the atomic models of the apo (grey) and 5' vRNA-bound (colored by domain) states. Regions exhibiting significant structural differences—the vRBL (1), fingers (2) and arch (3) domains—are highlighted with dashed boxes in (**a**) and (**b**). **c** Structural superposition of the vRBL (magenta) and fingers (orange) domains from the RNA-bound state with the apo state (grey), highlighting the stabilization of flexible regions upon RNA binding. d Detailed comparison of the 5' vRNA binding pocket. Up: overall structural alignment of the 5' vRNA-bound (colored, opaque) and apo (grey, transparent) states. Bottom: close-up view of the key residues involved in vRNA binding. Side chains of interacting residues are shown as sticks and labeled; the RNA is shown as lime lines. **e** Electrostatic potential surface of the CCHFV L protein. The RNA-binding site is outlined with a solid black box and shown in the zoomed-in view . The 5' vRNA is depicted as a green cartoon. The electrostatic potential scale bar is shown below. **f** Structural comparison of the 5' vRNA binding pocket in CCHFV (this work) with HTNV (PDB 8C4T), LASV (PDB 7OJN), and LACV (PDB 5AMQ). The comparison demonstrates the conservation of the 5' vRNA binding mechanism across the *Bunyavirales* order. All structures are colored according to the CCHFV domain definitions, except for the unique pendant domain in LASV (colored forest green).

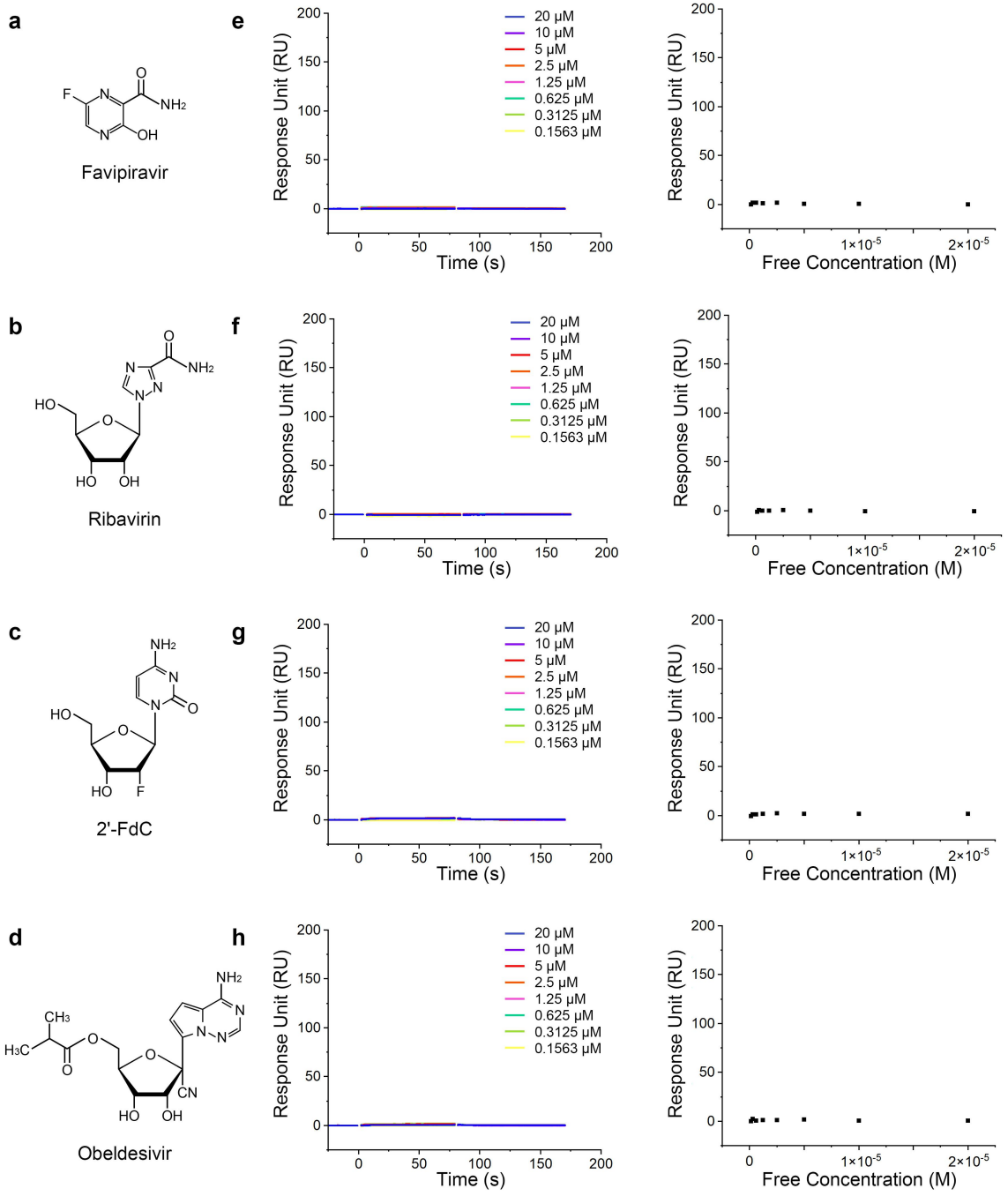

Supplementary Fig. 6: Affinity of nucleotide analogues for the CCHFV L protein. **a**–**b** Chemical structures of the antiviral nucleotide analogues tested: favipiravir (**a**), ribavirin (**b**), 2'-FdC (**c**) and obeldesivir (**d**). **e**–**h** Surface plasmon resonance (SPR) sensorgrams (left) and steady-state affinity fits (right) demonstrating that these compounds exhibit no significant binding to the CCHFV L protein at concentrations up to 20 μM, in contrast to the high affinity observed for suramin. Data are representative of *n* = 3 independent experiments.

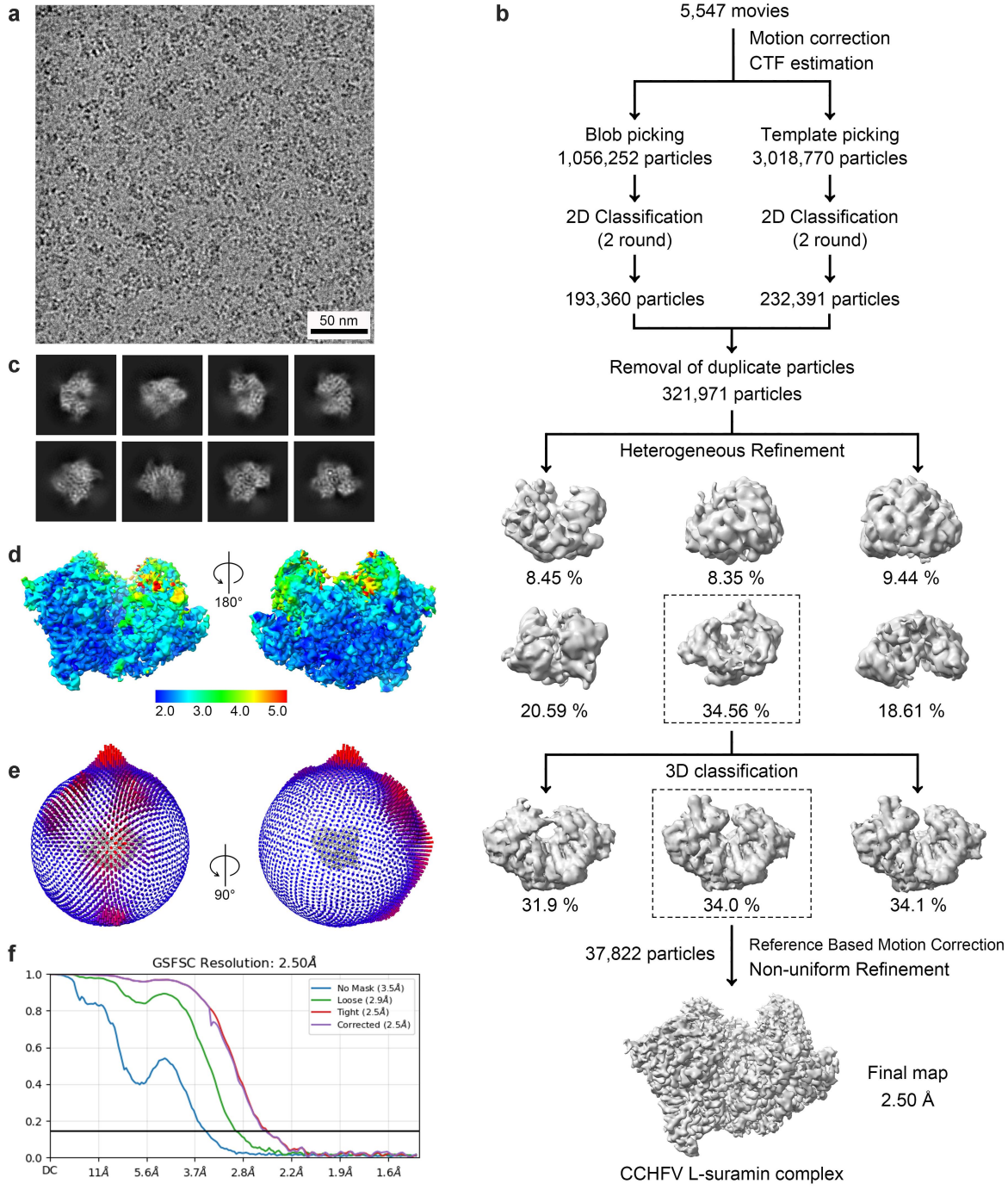

Supplementary Fig. 7: Cryo-EM data processing and reconstruction of the CCHFV L-suramin complex. a Representative cryo-EM micrograph of the CCHFV L-suramin complex. Scale bar, 50 nm. **b** Workflow of cryo-EM data processing. Particles were picked from 5,547 movies using blob and template-based strategies. Following 2D classification, heterogeneous refinement and 3D classification, a final set of 37,822 particles was subjected to non-uniform refinement, resulting in a density map at 2.50 Å resolution. **c** Representative 2D class averages of the L-suramin complex particles. **d** Local resolution map of the final reconstruction; the resolution color key is shown below. **e** Angular distribution of the particles used in the final reconstruction. **f** Gold-standard FSC curves indicating a final global resolution of 2.50 Å at the FSC = 0.143 threshold.

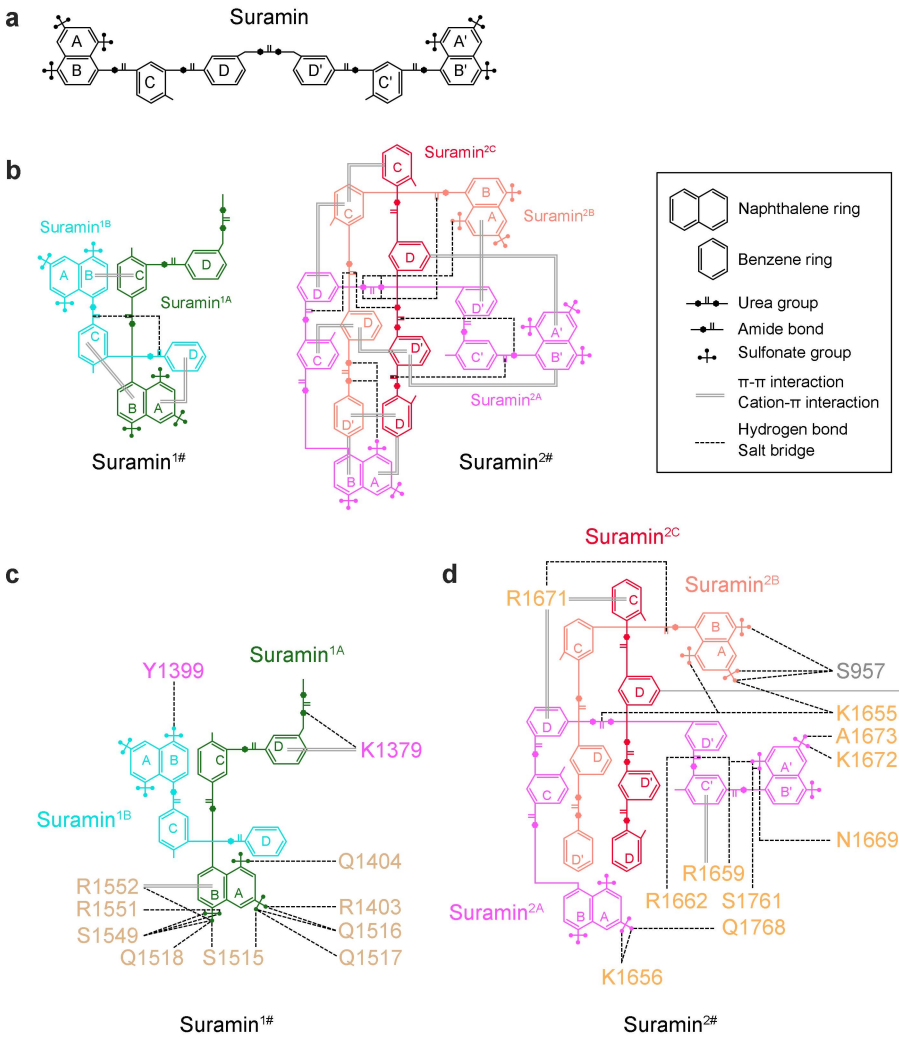

Supplementary Fig. 8: Schematic representation of interactions in the CCHFV L–suramin complex. a Chemical structure of the symmetrical suramin molecule. The naphthalene (A, B) and benzene (C, D) rings are labeled; primes (') denote the corresponding rings on the symmetrical side. **b** Intermolecular interactions between suramin molecules within the binding assemblies. Left: Site 1 (Suramin$^{1\#}$), showing interactions within the suramin dimer. Right: Site 2 (Suramin$^{2\#}$), showing interactions within the suramin trimer assembly. **c**–**d** Schematic representations of the interactions between the L protein and two suramin assemblies. Only amino acid residues involved in direct interactions are shown. Hydrogen bonds and salt bridges are indicated by black dashed lines. π–π interactions (in **b**) and cation–π interactions (in **c** and **d**) are depicted as grey double lines. The coloring of suramin molecules and protein residues is consistent with the main text figures.

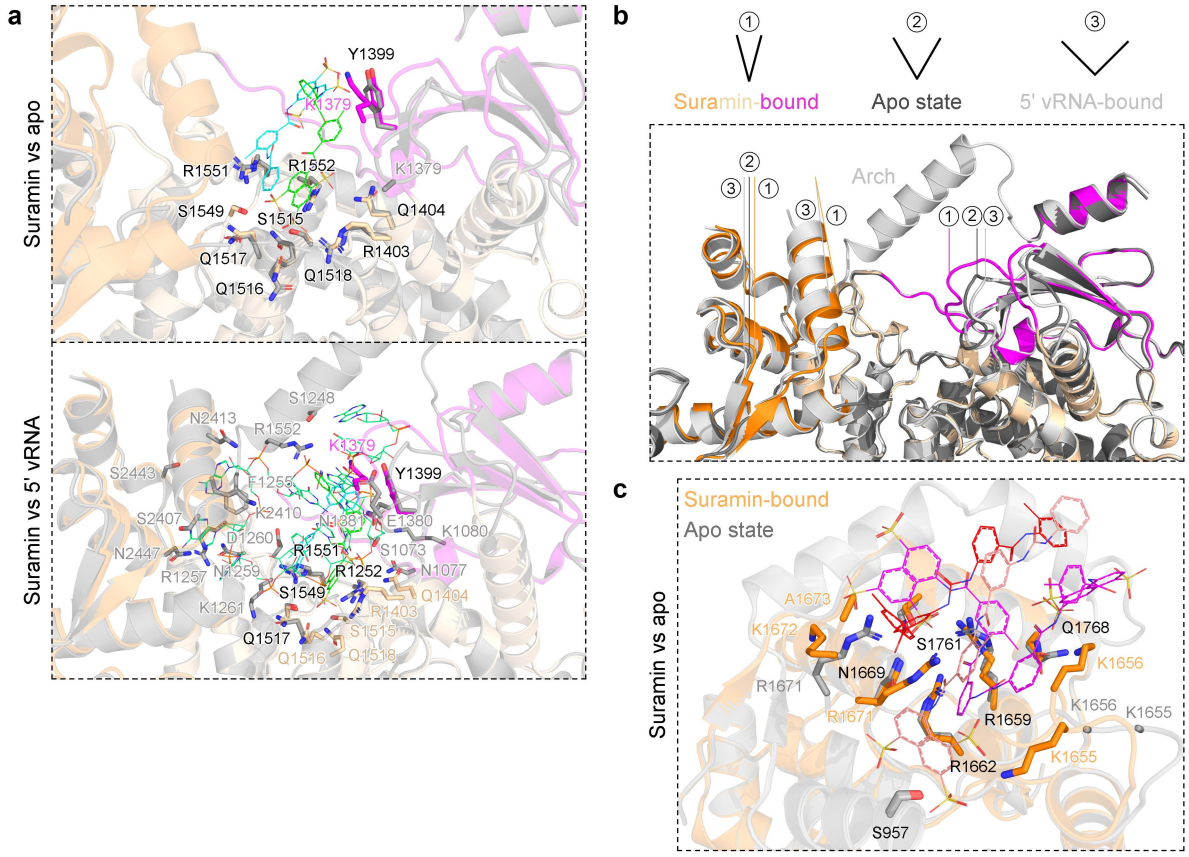

Supplementary Fig. 9: Conformational analysis of residues at the suramin–L protein interface. a Structural superposition of the suramin-bound state with the apo state (up) and the RNA-bound state (bottom) at Site 1 (Suramin$^{1\#}$). Residue K1379 undergoes a significant conformational shift, pulling the adjacent loop towards the inhibitor. Other residues involved in suramin binding exhibit minimal structural changes compared to the apo or RNA-bound states. However, the comparison in bottom confirms that suramin physically occupies the RNA-binding pocket, creating severe steric clashes. Residues R1252, Y1399, Q1517, S1549 and R1551 are shared recognition residues for both suramin and the 5' vRNA. **b** Structural superposition of the suramin-bound (colored), apo (black), and 5' vRNA-bound (grey) states. Relative to the apo state, RNA binding induces a slight expansion of the architecture, whereas suramin binding causes contraction. Labels 1, 2 and 3 indicate the relative positions of the same site in the suramin-bound, apo and RNA-bound states, respectively. **c** Superposition of the Suramin-bound and apo states at Site 2 (Suramin$^{2\#}$). Suramin binding stabilizes residues K1672 and A1673, and induces conformational changes in K1655, K1656 and R1671. The engagement of K1655 and K1656 specifically triggers a shift of the hosting loop towards the drug, while other residues remain largely unchanged.

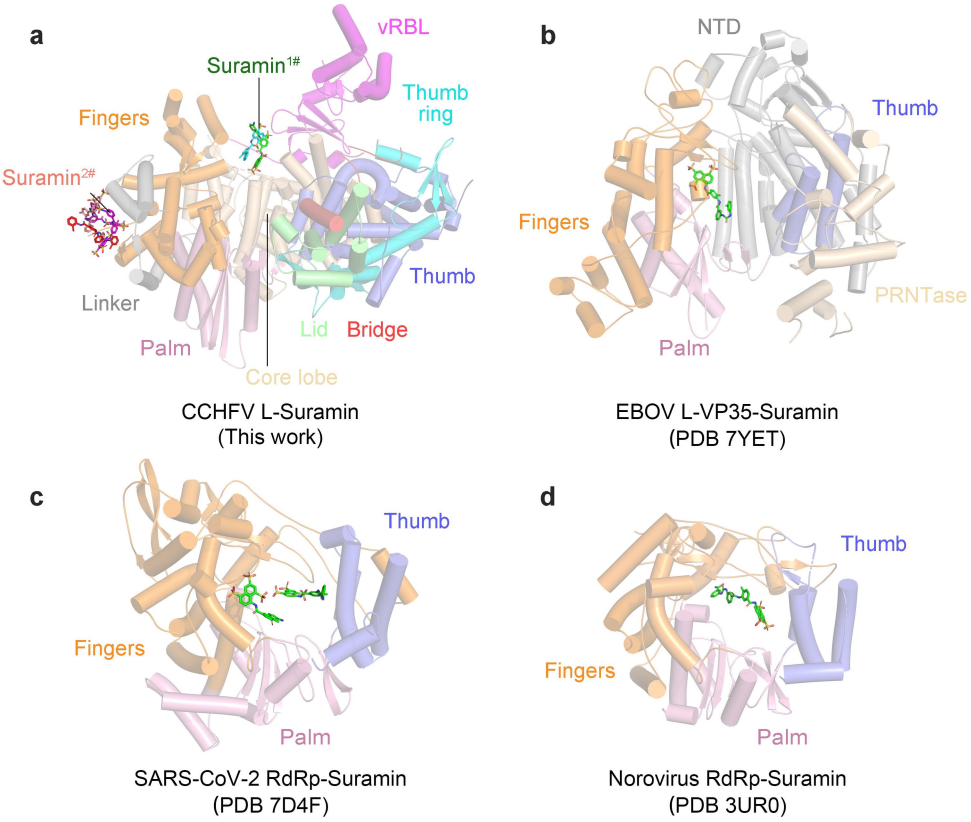

Supplementary Fig. 10: Comparison of suramin binding and inhibition mechanisms across viral RNA polymerases. a Structure of the CCHFV L protein bound to suramin (this work), showing the dual binding sites: Suramin$^{1\#}$ within the 5' vRNA binding pocket and Suramin$^{2\#}$ on the exterior surface of the linker–fingers domains. **b** Suramin binding to the Ebola virus (EBOV) L–VP35 polymerase complex (PDB 7YET). Suramin binds within the NTP entry channel, physically blocking the entry of substrates into the active site. **c** Suramin binding to the SARS-CoV-2 RdRp (PDB 7D4F). Two suramin molecules bind within the catalytic chamber, blocking the binding of both the RNA template and primer strands. **d** Suramin binding to the Norovirus RdRp (PDB 3UR0). Suramin binds in the cleft between the fingers and thumb domains, preventing the positioning of the RNA template for initiation. The comparison highlights that the binding sites and inhibition mechanism identified in the CCHFV L protein are distinct from the active-site or channel-blocking mechanisms reported for other viral polymerases. Proteins are shown as transparent cartoons colored by domain (corresponding to the CCHFV structure); suramin is shown as green sticks.

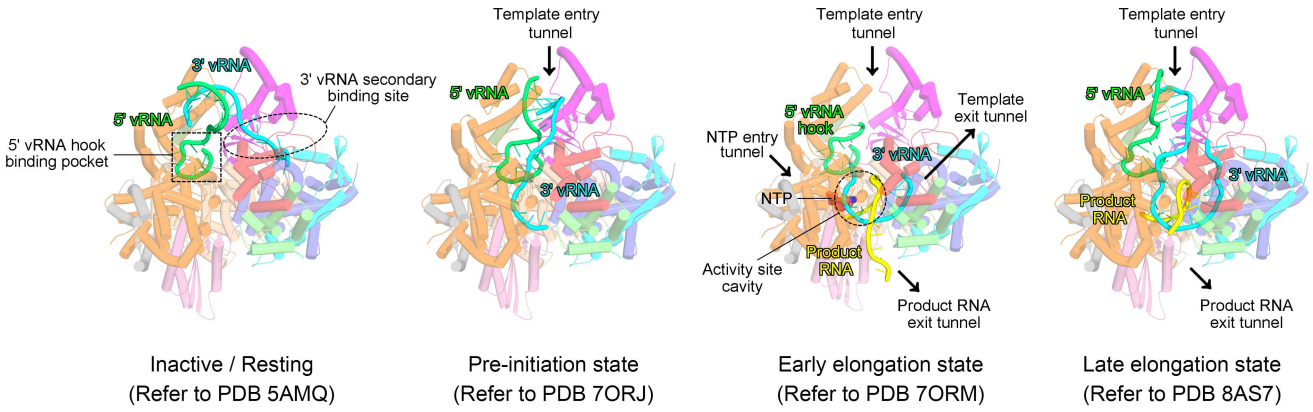

Supplementary Fig. 11: Structural model of the CCHFV L protein replication cycle. Proposed conformational states of the CCHFV L protein during the viral replication cycle, modeled on homologous structures from the *Bunyavirales* order. The cycle transitions from the inactive or resting state (based on PDB 5AMQ) to the pre-initiation state (based on PDB 7ORJ), in which the 5' vRNA hook is bound. Subsequent stages include the early elongation state (based on PDB 7ORM), showing product RNA formation, and the late elongation state (based on PDB 8AS7), where the product exits the polymerase. The paths of the 5' vRNA hook (green), 3' vRNA template (cyan) and product RNA (yellow) are indicated. Incoming NTPs are depicted as red spheres, and the location of the active site is marked.